REVIEW ARTICLE

Functional photoacoustic microscopy of hemodynamics: a review

Chao Liu[1,2] · Lidai Wang[1,2]

Abstract

Functional blood imaging can reflect tissue metabolism and organ viability, which is important for life science and biomedical studies. However, conventional imaging modalities either cannot provide sufficient contrast or cannot support simultaneous multi-functional imaging for hemodynamics. Photoacoustic imaging, as a hybrid imaging modality, can provide sufficient optical contrast and high spatial resolution, making it a powerful tool for in vivo vascular imaging. By using the optical-acoustic confocal alignment, photoacoustic imaging can even provide subcellular insight, referred as optical-resolution photoacoustic microscopy (OR-PAM). Based on a multi-wavelength laser source and developed the calculation methods, OR-PAM can provide multi-functional hemodynamic microscopic imaging of the total hemoglobin concentration (C_{Hb}), oxygen saturation (sO_2), blood flow (BF), partial oxygen pressure (pO_2), oxygen extraction fraction, and metabolic rate of oxygen (MRO_2). This concise review aims to systematically introduce the principles and methods to acquire various functional parameters for hemodynamics by photoacoustic microscopy in recent studies, with characteristics and advantages comparison, typical biomedical applications introduction, and future outlook discussion.

Keywords Photoacoustic imaging · Multi-functional imaging · Hemodynamics · Calculation methods

1 Introduction

Functional blood imaging signifies its uniqueness for acquiring the physiological activities of hemodynamics, including the total hemoglobin concentration (C_{Hb}) [1, 2], oxygen saturation (sO_2) [3, 4], blood flow (BF) [5, 6], partial oxygen pressure (pO_2) [7, 8], oxygen extraction fraction (OEF) [9, 10], and metabolic rate of oxygen (MRO_2) [11, 12], making it a powerful tool for blood related biomedical applications [13–15]. Up to now, many imaging modalities have been used for functional blood imaging, for instance, the positron emission tomography (PET) [16], functional computed tomography (fCT) [17], functional magnetic resonance imaging (fMRI) [18], and functional near-infrared spectroscopy (fNIRS) [19]. However, all these imaging technics either cannot provide sufficient contrast or cannot support simultaneous multi-functional imaging. Table 1 shows the comparison of conventional biomedical imaging modalities. A new imaging technic providing multiple functional applications for hemodynamics with high contrast is in high demand.

As a hybrid imaging technic develops for less than 30 years, photoacoustic imaging has attracted worldwide attention for its potential in biomedical research [20, 25–47]. Photoacoustic imaging is based on the target's intrinsic absorption property, with the principle that when the target is shone by the pulsed light, the light will be absorbed and converted into heat, which causes initial pressure rise as ultrasonic wave (also named as a photoacoustic wave) [20, 25]. By using the ultrasonic transducer to collect the generated ultrasonic wave, the photoacoustic image can be reconstructed, which reflects the optical absorption deposition in biological tissue [20, 25]. In another word, Photoacoustic imaging can let us listen to the sound of light and see the color of biological tissue itself. Photoacoustic imaging combines optical excitation and ultrasound detection, bringing itself the advantages of high optical contrast and low ultrasonic scattering at the same time. Photoacoustic imaging is also a suitable tool to perform functional imaging. Since

✉ Lidai Wang
   lidawang@cityu.edu.hk

1 Department of Biomedical Engineering, City University of Hong Kong, 83 Tat Chee Ave, Kowloon, Hong Kong SAR, China

2 City University of Hong Kong Shenzhen Research Institute, Yuexing Yi Dao, Nanshan District, Shenzhen 518057, Guang Dong, China

Table 1 Comparison of conventional biomedical imaging modalities [20–24]

BIM	PAI	fMRI	OCT	PET	USI	fNIRS	fCT
Mechanism	Optical absorption and acoustic detection	Magnetic waves	Optical waves	Photons emitted by radioactive tracer	Acoustic waves	Optical absorption (molecular overtone)	X-rays
Imaging contrast	Optical and acoustic properties	Magnetic property	Optical property	Radioactive tracer's property	Acoustic property	Optical property	X-rays attenuation coefficient
Penetration depth	~1 mm for OR-PAM ~50 mm for PACT	cm (whole body)	~1 mm	~10 mm	cm (whole body)	~10 mm	cm (whole body)
Imaging resolution	~3 µm for OR-PAM ~100 µm for PACT	10–100 µm	~10 µm	~1 mm	~0.3 mm	~10 mm	50–200 µm
Functional availability	C_{Hb}, sO_2, BF, pO_2, OEF, MrO_2	C_{Hb}, sO_2, BF, pO_2, OEF, MrO_2	C_{Hb}, sO_2, BF, pO_2, OEF, MrO_2	sO_2, BF, pO_2, OEF, MrO_2	BF	C_{Hb}, sO_2, BF, pO_2, OEF, MrO_2	BF
Advantages	Excellent and scalable SR and PD High optical contrast Weak SA	High SR Good soft-tissue contrast Support imaging of brain activity	Very High SR High SNR Suitable for thick target	High PD Support imaging of brain activity	Very high PD Inexpensive Widely use	Portable Inexpensive	Support bone imaging Very high PD Good SR
Limitations	Low PD for OR-PAM Low SR for PACT	Cost Low S	Limited PD Strong SA	Low SR Radiation risk Cost	Low S Low SR Strong SA	Low SR Limited PD	Poor soft-tissue contrast Radiation risk

BIM biomedical imaging modalities, *OCT* optical coherence tomography, *PAI* photoacoustic imaging, *PACT* photoacoustic computed tomography, *PD* penetration depth, *SR* spatial resolution, *S* sensitivity, *SA* speckle artifacts, *USI* ultrasound imaging

the photoacoustic imaging can reflect the excitation wavelength's absorption distribution in biological tissue, multiple wavelengths can be used with developed calculation methods to acquire the multiple functional information including C_{Hb} [48], sO_2 [49], BF [50], pO_2 [51], OEF [52], and MRO_2 [53], shown in Fig. 1. Taking advantages of optical-resolution photoacoustic microscopy (OR-PAM),photoacoustic imaging can even provide functional imaging with optical resolution [21, 54–61].

This review introduces the principles and multiple methods to acquire the various above hemodynamic related functional information based on photoacoustic microscopy, and their related biomedical applications. C_{Hb} can reflect the vascular structure and blood perfusion. By using the isosbestic wavelengths of hemoglobin, relative C_{Hb} can be reflected directly through photoacoustic amplitude regardless of the sO_2 variation. The sO_2 signifies the tissue oxygenation condition, which can be calculated by linear and nonlinear methods based on photoacoustic imaging. And the sO_2 can be further calibrated to increase the accuracy based on the optical or acoustic compensation. BF can be calculated by photoacoustic flowmetry through various principles including direct, optical encoding, target correlation, and thermal tagging measurement methods. They have different characteristics and advantages. The pO_2 indicates the balance

between oxygen delivery and its consumption, which can be acquired by measuring the lifetime of injected oxygen-sensitive dye using photoacoustic imaging. OEF reflects the tissue ability to obtain oxygen from the blood, which is important to maintain vascular function and morphological integrity. It can be acquired by subtracting the sO_2 in draining veins from that in feeding arteries in the region of interest (ROI). The MRO_2 can directly reflect the tissue oxygen consumption and energy utilization which can be calculated by combining the OEF, BF, and C_{Hb}. It has been used as an indicator of tissue viability and function in various vital biomedical applications, for instance, brain activities and tumor development study. Photoacoustic imaging can provide multiple functional imaging and sufficient optical contrast for hemodynamic activities, making it a potential imaging tool for preclinical and clinical applications in the future.

2 Hemoglobin concentration

The C_{Hb} in the blood is an important indicator for health condition, and meanwhile, it is also a good absorber for wavelengths near the 500 nm range [21]. Owing to the high background contrast offered by photoacoustic imaging, C_{Hb} imaging can manifest the blood vessels' structure. It helps a
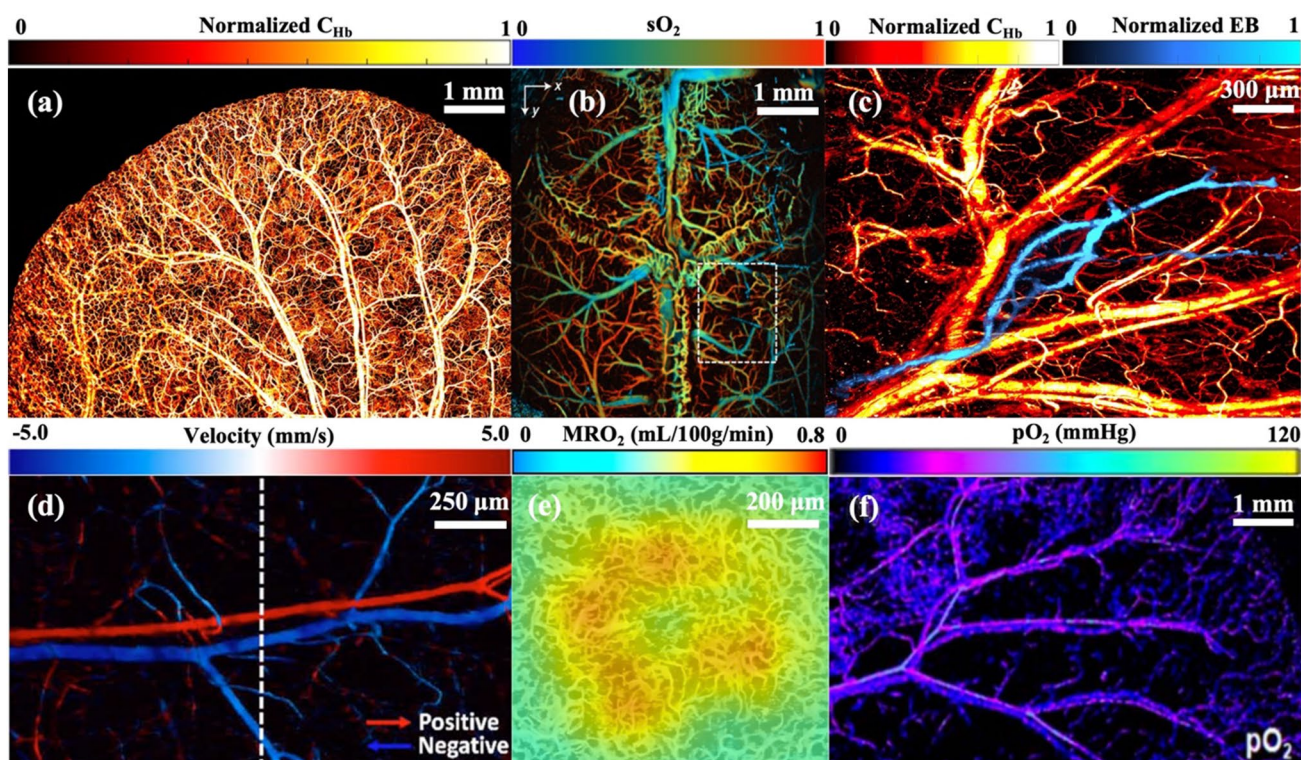
Fig. 1 Functional in vivo photoacoustic imaging of **a** normalized C_{Hb} in mouse ear [62], **b** sO_2 in mouse brain with intact skull [63], **c** blood vessel and Evans Blue-labeled lymphatic vessels [55], **d** Blood flow velocities with direction [64], **e** MRO_2 of mouse kidney in acute kidney injury model [65], and **f** pO_2 in the mouse ear [66]. All figures are reprinted with permission

lot for early cancer imaging diagnosis since angiogenesis is the hallmark of early cancer [67].

The linear expression for acquiring the magnitude of the PA signal from blood can be calculated as [20, 21]:

$$PA = k\Gamma\eta F\mu_a$$

$$\mu_a = \beta C_{Hb}\left[sO_2\varepsilon^{HbO_2} + \left(1 - sO_2\right)\varepsilon^{HbR}\right], \tag{1}$$

where k is a constant reflecting the photoacoustic detection sensitivity; Γ is the Grueneisen parameter indicating the thermal related property of absorber; η represents the conversion percentage from absorbed light to heat; F denotes the local optical fluence; μ_a signifies the absorption coefficient of the absorber which is also related with wavelength; β is a fixed constant [20]; C_{Hb} is the total hemoglobin concentration; ε^{HbR} and ε^{HbO_2} signify the molar extinction coefficients of deoxygenated hemoglobin (HbR) and oxygenated hemoglobin (HbO$_2$) respectively at the exciting wavelength. Thus, by selecting the isosbestic wavelengths for hemoglobin (which means the ε^{HbR} and ε^{HbO_2} are nearly the same), the photoacoustic signals will be independent of sO$_2$ and are only dependent by C$_{Hb}$ as

$$C_{Hb} \propto PA, \tag{2}$$

Thus, by selecting the isosbestic wavelengths for hemoglobin (which means the ε^{HbO_2} and ε^{HbR} are nearly the same), the C$_{Hb}$ can be normalized by the amplitude of photoacoustic signals. The typical isosbestic wavelengths for hemoglobin near 500 nm range are 498, 545, 570, and 584 nm [21, 54]. By selecting such isosbestic wavelengths, the total hemoglobin concentration or normalized total hemoglobin concentration can be acquired by single-wavelength photoacoustic imaging.

3 Oxygen saturation

The sO$_2$ is an important physiological parameter mirroring the respiratory circulation status and creature viability [49]. Several sO$_2$ measuring methods are developed based on photoacoustic imaging including linear [37, 59, 63, 67–73] and nonlinear methods [74, 75]. Furthermore, sO$_2$ compensation methods are also developed to improve the sO$_2$ measuring accuracy for different situations [62, 76, 77]. Table 2 shows the summary of the attributes of various photoacoustic imaging techniques for sO$_2$.

3.1 *Linear method for sO$_2$*

The conventional sO$_2$ measurement by photoacoustic imaging is a linear method, which needs two different wavelengths (they can't both be the isosbestic wavelengths

for hemoglobin) to do spectral unmixing calculation [37, 59, 63, 67–73]. Based on Eq. (1), by using two wavelengths, we can acquire both photoacoustic signals as follows:

$$PA_1 = k\Gamma\eta F_1\beta C_{Hb}\left[sO_2\varepsilon_1^{HbO_2} + \left(1 - sO_2\right)\varepsilon_1^{HbR}\right]$$

$$PA_2 = k\Gamma\eta F_2\beta C_{Hb}\left[sO_2\varepsilon_2^{HbO_2} + \left(1 - sO_2\right)\varepsilon_2^{HbR}\right], \tag{3}$$

By combing two equations in Eq. (3), we can acquire the sO$_2$ as:

$$sO_2 = \frac{\varepsilon_2^{HbR} - \rho\varepsilon_1^{HbR}}{(\varepsilon_2^{HbR} - \varepsilon_2^{HbO_2}) - \rho(\varepsilon_1^{HbR} - \varepsilon_1^{HbO_2})}, \tag{4}$$

where $\rho = \frac{F_1 \cdot PA_2}{F_2 \cdot PA_1}$, $F_{1,2}$ and $PA_{1,2}$ denote optical fluence and photoacoustic amplitudes at these two excitation wavelengths, and $\varepsilon_{1,2}^{HbO_2}$ and $\varepsilon_{1,2}^{HbR}$ are known constant. After obtaining the optical fluence and photoacoustic amplitudes from both wavelengths, the sO$_2$ can be acquired. Many researchers have acquired the sO$_2$ mapping via this method shown in Fig. 2, the differences are the wavelengths they chose and the way they build up the dual-wavelength measuring method.

The direct way is to use two laser sources with controlled time delay by an external trigger, shown in Fig. 2a, b [73]. To realize the in vivo functional brain imaging, Yao et al. [63] developed a dual-wavelength OR-PAM, which consists of a dye laser at 610 nm (which is pumped by a 532-nm pulsed laser beam with 3-ns pulse width) and another 3-ns pulsed laser at 532 nm. Longer wavelength suffers from less optical scattering problem in biological tissue, compared with other wavelengths in 500-nm range, 610 nm can be an optimal choice for deep brain imaging, shown in Fig. 1b. However using two independent laser sources not only increases system cost but also inevitably suffers from pulse fluctuations problem, which may cause an error for sO$_2$ calculation. To solve this problem, in 2014, Hajireza et al. [78] harnessed stimulated Raman scattering (SRS) effect from optical fiber to build up the multi-spectral OR-PAM. By pumping the pulsed low-order wavelength as seed (e.g. 532 nm), the high-order Stokes wavelengths can be generated (e.g. 545, 558 nm). Because they are homologous from the same pump laser source, the pulse fluctuations problem can be relieved. In 2016, based on SRS effect, Wang et al. [69] used an electro-optical modulator (EOM) to build up a pulse-by-pulse-switching dual-wavelength OR-PAM, which achieves 300-kHz A-line rate and increases the imaging speed 20 times faster than previous work, shown in Fig. 2c–d. However, the time delay between the two wavelengths is limited by

Table 2 Summary of the attributes of photoacoustic imaging techniques for sO$_2$

Method	Principle	Wavelength used (nm)	Advantages	Shortcomings
L by multiple lasers [63]	Spectral unmixing	532, 610	Easy Setup	System cost
L by EOM [69]	Spectral unmixing	532, 558	High A-line rate at 300-kHz	Misalignment in adjacent points
L by fiber-based SRS [70]	Spectral unmixing	532, 558	Ultrashort switching time at sub-microsecond level	Bare adequate energy threshold; Energy fluctuation for Raman pulse
L by crystal-based SRS [71]	Spectral unmixing	532, 558	Low pulse energy fluctuation	System cost
N by intensity saturation [74]	Different absorption lifetime for HbO$_2$ and HbR	576	Single wavelength reduces wavelength-dependent optical attenuation	High laser intensity changes Grüneisen parameter, leading to measurement error
N by different pulse width [75]	Different absorption saturation for nanosecond and picosecond pulse width	532	Single wavelength reduces optical scattering; Shorter wavelength requires low laser intensity	Weak saturation in deep tissue limits the imaging depth
C for saturation effect [62]	Absorption saturation makes PA signals nonlinear to μ_a	532, 545, 558	Effective when μ_a is high or Δz is low	Less effect for small blood vessels
C for optical scattering [76]	Optical scattering in tissue causes significant attenuation to F	532, 545, 558	More effective for small vessel	Sensitive to measurement noise
C for acoustic attenuation [77]	Different sizes of blood vessels lead to nonuniform spectral response	532, 558	Remove the attenuation from vessel diameter and pulse width; Improve the sO$_2$ accuracy by ~ 15%	Loss of phase information to completely restore the original

L, N, and C are short for linear, nonlinear and compensation sO$_2$ measurements, respectively
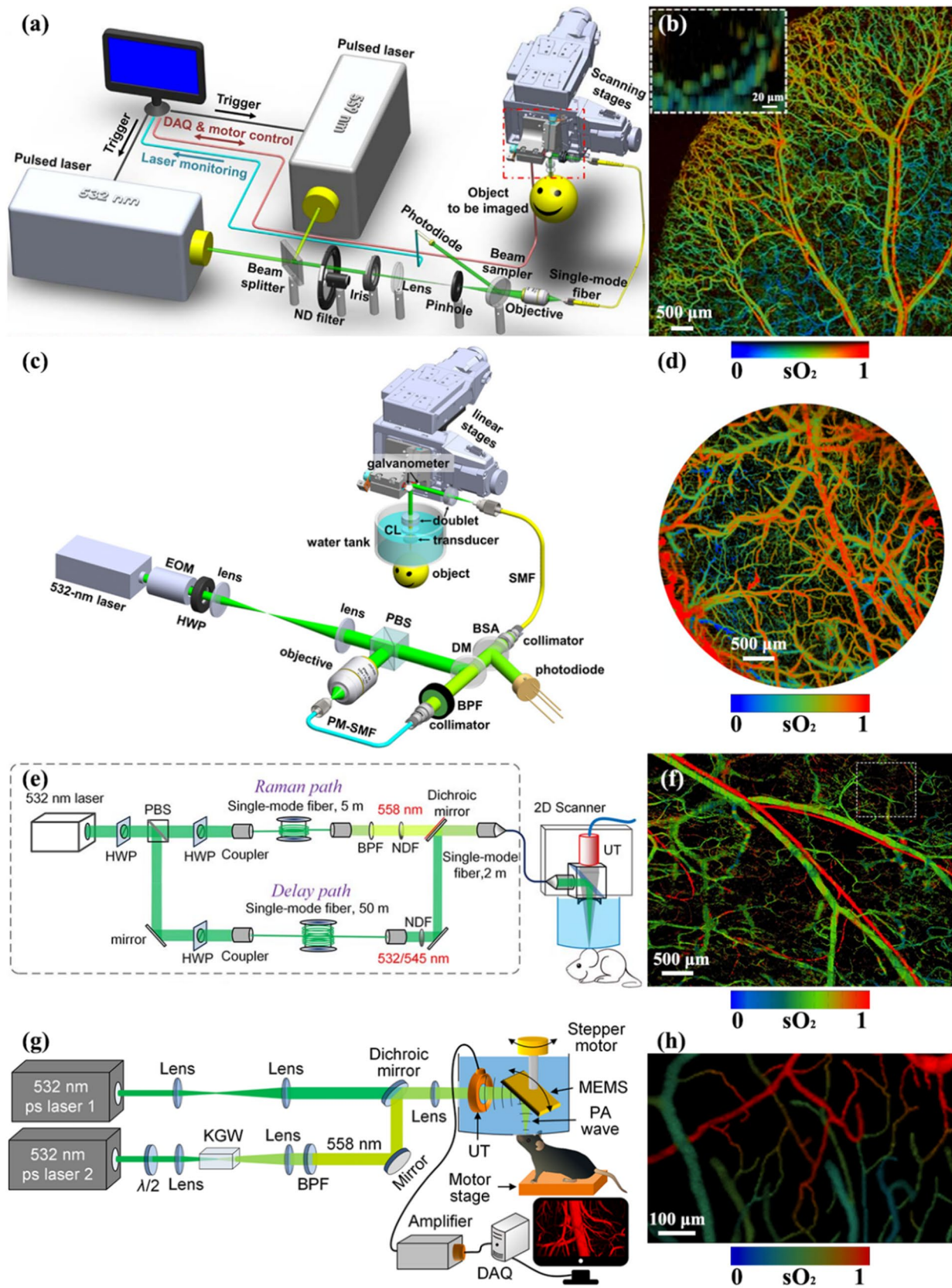
Fig. 2 The system **a–g** and corresponding sO$_2$ imaging results **b–h** for linear sO$_2$ methods: two laser sources [73] and single laser source with EOM [69], fiber-based SRS [70], and crystal-based SRS [71]. All figures are reprinted with permission

the laser repetition frequency. It may be a problem when increasing the scanning speed because the increased step size of the scanned A-line may cause severer misalignment between the optical focal spots of the dual wavelengths. It can induce considerable errors in sO$_2$ mapping. To solve this, Liang et al. developed a 2-MHz dual-wavelength system with ultrashort 220 ns pulse switching time, which is realized by the fiber delay, shown in Fig. 2e, [70]. In this work, Liang uses different optical fiber lengths for normal light path and SRS light path, so the time delay between two different pulses is decided by the fiber lengths, which can reduce the switching time to sub-microsecond level. The ultrashort switching time enables high accurate functional photoacoustic imaging, demonstrated in this work by detecting the sO$_2$ gradual change from red blood cells when flowing from arterioles to venules, shown in Fig. 2f. Although fiber-based SRS enables short and changeable switching time, it also has limitations. One problem is the broader linewidth for higher-order SRS wavelength, which may induce error in calculation. The other problem is the limited SRS energy threshold, which is inversely related to the fiber length. Adequate delay time among different pulses needs enough length of the fiber, which may restrict the output energy of SRS wavelength for photoacoustic sensing. In 2020, He et al. developed a crystal-based SRS dual-wavelength OR-PAM for functional brain imaging shown in Fig. 2g, h, [71]. In his work, a potassium gadolinium tungstate crystal was used to conduct SRS. For Raman wavelength 558 nm, a short linewidth with ~ 0.5 nm and high pulsed energy of ~150 nJ was acquired to satisfy the photoacoustic sensing. The deviation of relative pulse energy fluctuation was also measured to be 1.64%, which is rather smaller than the fiber-based SRS optical path. The work from Hosseinaee et al. indicated a lower temperature can elevate the fiber-based SRS stability [72]. However, this system requires two picosecond-pulsed lasers, which increases the system cost greatly.

3.2 Nonlinear method for sO$_2$

3.2.1 Nonlinear method based on intensity saturation

Linear sO$_2$ measurement requires at least two different wavelengths, which may cause the wavelength-dependent optical attenuation for incident fluence, and further induce error in sO$_2$ calculation. One solution is to use the same wavelength to map sO$_2$. In 2011, Danielli et al. developed single-wavelength photoacoustic microscopy based on absorption saturation, shown in Fig. 3a–e, [74]. Many previous functional photoacoustic studies have described the linear correlation between photoacoustic signal amplitude and local light fluence. However, Danielli found when the light intensity gets stronger, the optical absorption saturation

will happen, leading to a nonlinear relationship between the photoacoustic signal and local optical fluence. It is caused by the different absorption lifetime of different hemoglobin (HbO$_2$ and HbR) [79]. Different from the common μ_a expression as Eq. (1), when absorption happens, the $\mu_a(I)$ will saturate with the increasing intensity and should be rewritten as follows:

$$\mu_a(I) = \sigma_{HbO_2} \cdot \frac{A_{HbO_2}}{1 + \frac{I}{I_{sat}^{HbO_2}}} + \sigma_{HbR} \cdot \frac{A_{HbR}}{1 + \frac{I}{I_{sat}^{HbR}}}$$

$$F = I \cdot \tau_{laser}, \tag{5}$$

where σ_{HbO_2} and σ_{HbR}, A_{HbO_2} and A_{HbR}, $I_{sat}^{HbO_2}$ and I_{sat}^{HbR} are respectively the absorption cross-section of the absorber, amount of absorber, and optical intensity when saturation happens for HbO_2 and HbR in each unit volume, I is the optical intensity, F is the local optical fluence, and τ_{laser} is the pulse width of the laser source. After combining Eq. (1) and (5), we obtain

$$PA = k\Gamma\eta \cdot \left[\sigma_{HbO_2} \cdot \frac{A_{HbO_2}}{1 + \frac{F}{\tau_{laser} \cdot I_{sat}^{HbO_2}}} \cdot F + \sigma_{HbR} \cdot \frac{A_{HbR}}{1 + \frac{F}{\tau_{laser} \cdot I_{sat}^{HbR}}} \cdot F \right], \tag{6}$$

Thus, by applying different optical fluence, the relative concentration of HbO_2 and HbR can be acquired by Eq. (6), and the sO$_2$ can be calculated from:

$$sO_2 = \frac{A_{HbO_2}}{A_{HbO_2} + A_{HbR}}, \tag{7}$$

3.2.2 Nonlinear method based on different pulse width

Based on the sample absorption saturation principle, Yao et al. also developed a pulse-width-based sO$_2$ (PW-sO$_2$) measurement via a single wavelength in 2015, shown in Fig. 3f–k, [75]. In this work, a two-laser sources including one picosecond and one nanosecond laser source are used to demonstrate different absorption saturation to HbO_2 and HbR. The experimental results show that when light intensity elevates, the picosecond laser source can cause stronger saturation to HbO_2 compared with the picosecond laser source. On the contrary, HbR reflects similarly to two different laser pulses. Yao et al. set the same pulsed energy for these two lasers with different pulse widths. So when saturation just happens using a picosecond laser, there will be no saturation happening via nanosecond laser. Thus the photoacoustic signals from nanosecond and picosecond.
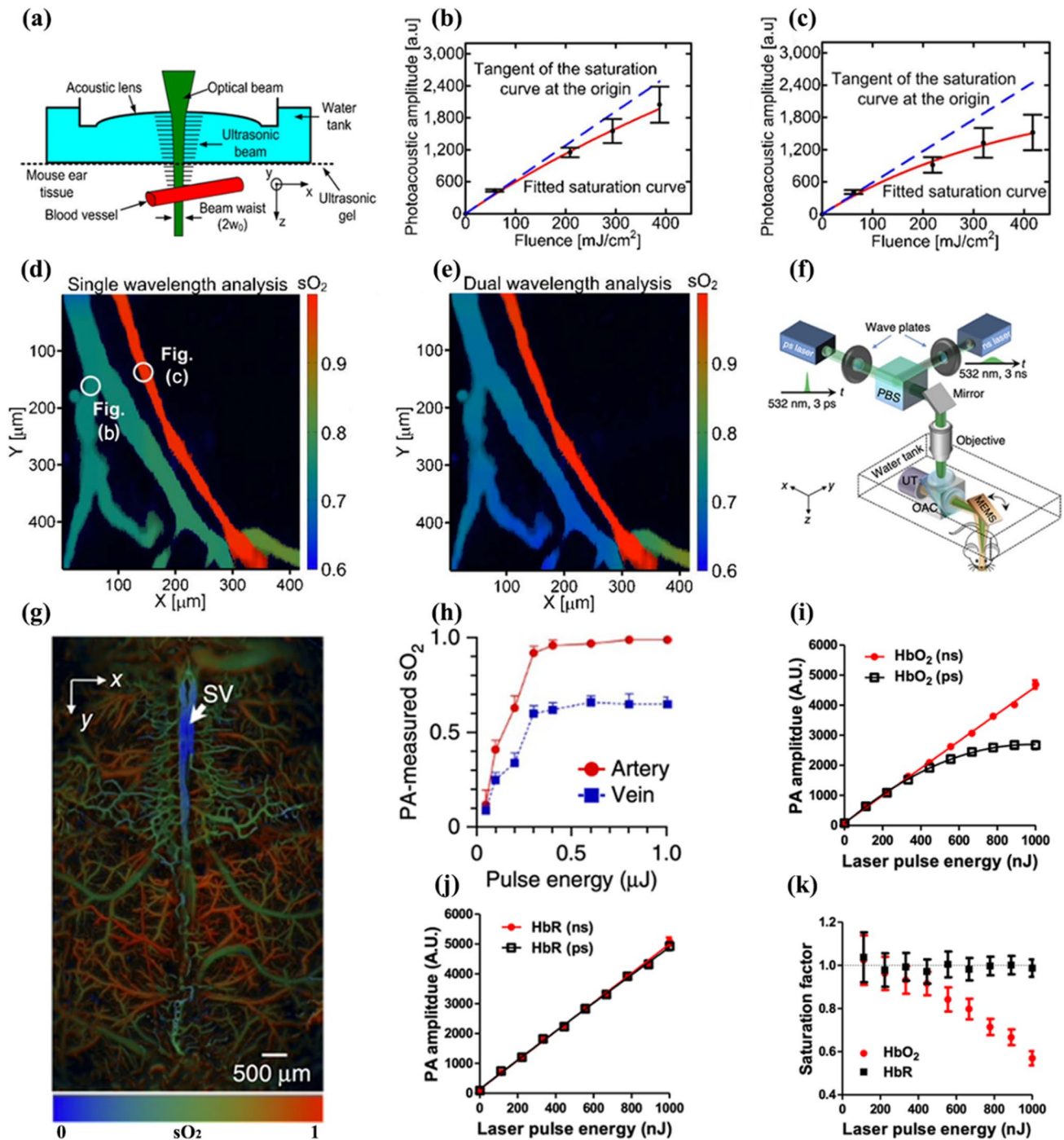
Fig. 3 **a–e** The nonlinear sO$_2$ measurement method based on intensity saturation [74]; **a** is the diagram for single wavelength imaging; **b–c** respectively show the average photoacoustic amplitude as a function of the fluence in vein and artery in nonlinear sO$_2$ result (**d**); **e** Shows the linear sO$_2$ result by a conventional dual-wavelength method. **f–k** Signifies the nonlinear sO$_2$ measurement method based on different pulse width [75]; **f** is picosecond/nanosecond single-wavelength system diagram; **g** is the nonlinear sO$_2$ brain imaging; **h** shows the in vivo nonlinear sO$_2$ results in an artery-vein pair in a mouse ear with different pulse energies; **i** and **j** are photoacoustic amplitudes of HbO$_2$ and HbR under different picosecond and nanosecond pulse energies; **k** demonstrates the saturation factor for HbO$_2$ and HbR under different pulsed energy, which is defined as the ratio of the photoacoustic amplitude with picosecond excitation to that with nanosecond excitation. All figures are reprinted with permission

pulses can be expressed as [75]:

$$PA_{ps} = k\Gamma\eta F\beta C_{Hb}\big[sO_2\varepsilon^{HbO_2} \cdot r_{HbO_2} + \big(1 - sO_2\big)\varepsilon^{HbR} \cdot r_{HbR}\big]$$

$$PA_{ns} = k\Gamma\eta F\beta C_{Hb}\big[sO_2\varepsilon^{HbO_2} + \big(1 - sO_2\big)\varepsilon^{HbR}\big], \tag{8}$$

where r_{HbO_2} and r_{HbR} are the saturation factors of HbO_2 and HbR, respectively. Considering.

using the isosbestic wavelength, ε^{HbO_2} will equal to ε^{HbR} and $r_{HbR} \approx 1$. Thus by taking the ratio of Eqs. (8), the sO_2 can be estimated as:

$$sO_2 = \frac{1 - \frac{PA_{ps}}{PA_{ns}}}{1 - r_{HbO_2}}, \tag{9}$$

where r_{HbO_2} is estimated by local fluence F.

The saturation-based nonlinear sO_2 measuring method can reduce the calculation induced by wavelength-dependent optical attenuation compared with the normal multi-wavelength method. However, the imaging depth will be reduced because the optical attenuation will make the saturation weak at deep tissue. The maximum imaging depth for 532 nm via this nonlinear method will be ~0.5 mm.

3.3 Compensation for sO₂

3.3.1 Optical compensation

The existing sO_2 measuring methods are all more or less simplified for calculation. Considering the particular circumstances, the simplified method can induce significant error, making it necessary to compensate for sO_2 imaging.

Wang et al. [80] and Liu et al. [62] found when the absorption coefficient μ_a is too high or the axial resolution is too low, the acquired photoacoustic signal will not linearly reflect the optical absorption change, which is named as saturation effect. Different from the absorption saturation effect discussed in Chapter. 3.2.1 which is caused by absorption relaxation time, here the saturation effect describes a phenomenon that photoacoustic signal will only be decided by the pulsed energy and is independent of absorption coefficient change. Thus the traditional linear method cannot figure out precise sO_2 affected by this saturation effect.

A conventional method usually omits the ultrasonic transducer' finite bandwidth and assumes that the photoacoustic amplitude is linear to the product of fluence F and absorption coefficient μ_a as Eq. (1). However, when the axial resolution of the system is limited, the photoacoustic amplitude from a voxel should be written as:

$$PA = \int_0^{\Delta z} k\Gamma\eta F\mu_a \exp\big(-\mu_a z\big)dz$$
$$= k\Gamma\eta F\big[1 - \exp\big(-\mu_a\Delta z\big)\big], \tag{10}$$

where Δz is the voxel size in the axial direction. Thus, the photoacoustic amplitude will only be linear to fluence F and will be nonlinear to μ_a. Considering Eq. (1), the expression can be rewritten as:

$$PA = k\Gamma\eta F\big[1 - \exp\big(-\big(sO_2\varepsilon^{HbO_2} + \big(1 - sO_2\big)\varepsilon^{HbR}\big)rC_{Hb}\Delta z\big)\big], \tag{11}$$

There are three unknowns here: $k\Gamma\eta$, sO_2, and $rC_{Hb}\Delta z$. Thus by solving this equation, in 2019, Liu et al. [62] developed a nonlinear method for sO_2 compensation based on a triple-wavelength OR-PAM shown in Fig. 4a, b, g. Three wavelengths can build up to three nonlinear equations as Eq. (11) for solving the above three unknowns. An iterative algorithm is used in two steps for gradually getting the final sO_2 value. In the first step of ith iteration, the ratio of the photoacoustic signals generated by the first wavelength and the second wavelength can be calculated as:

$$\frac{PA_{1\_i}}{PA_{2\_i}} = \frac{1 - \exp\Big[-u_i\Big(sO_{2\_i}\varepsilon_1^{HbO_2} + \big(1 - sO_{2\_i}\big)\varepsilon_1^{HbR}\Big)\Big]}{1 - \exp\Big[-u_i\Big(sO_{2\_i}\varepsilon_2^{HbO_2} + \big(1 - sO_{2\_i}\big)\varepsilon_2^{HbR}\Big)\Big]}, \tag{12}$$

where $u_i = rC_{Hb_i}\Delta z_i$. Here sO_{2_i-1} in the previous iteration is substituted into Eq. (12) to figure out u_i. In the second step, u_i is substituted into the equation generated by the ratio of the photoacoustic signals from the third wavelength and the second wavelength as follows:

$$\frac{PA_{3\_i}}{PA_{2\_i}} = \frac{1 - \exp\Big[-u_i\Big(sO_{2\_i}\varepsilon_3^{HbO_2} + \big(1 - sO_{2\_i}\big)\varepsilon_3^{HbR}\Big)\Big]}{1 - \exp\Big[-u_i\Big(sO_{2\_i}\varepsilon_2^{HbO_2} + \big(1 - sO_{2\_i}\big)\varepsilon_2^{HbR}\Big)\Big]}, \tag{13}$$

Then the updated sO_{2_i} can be figured out. To start this iteration, the initial sO_{2_0} can be acquired from the conventional linear method. After obtaining the converged sO_2, the iteration is stopped. In this work, by imaging the mouse ear as a model, the sO_2 in arteries and veins can be compensated back to 19% and 7%, respectively. This method can compensate better in large vessels than in smaller vessels because the size of smaller vessels may be tinier than the

Fig. 4 **a–f** sO$_2$ imaging without and with compensation related to absorption saturation effect [62], optical scattering [76] and acoustic attenuation [77], and their comparison are shown in **g**, **i**, respectively. All figures are reprinted with permission
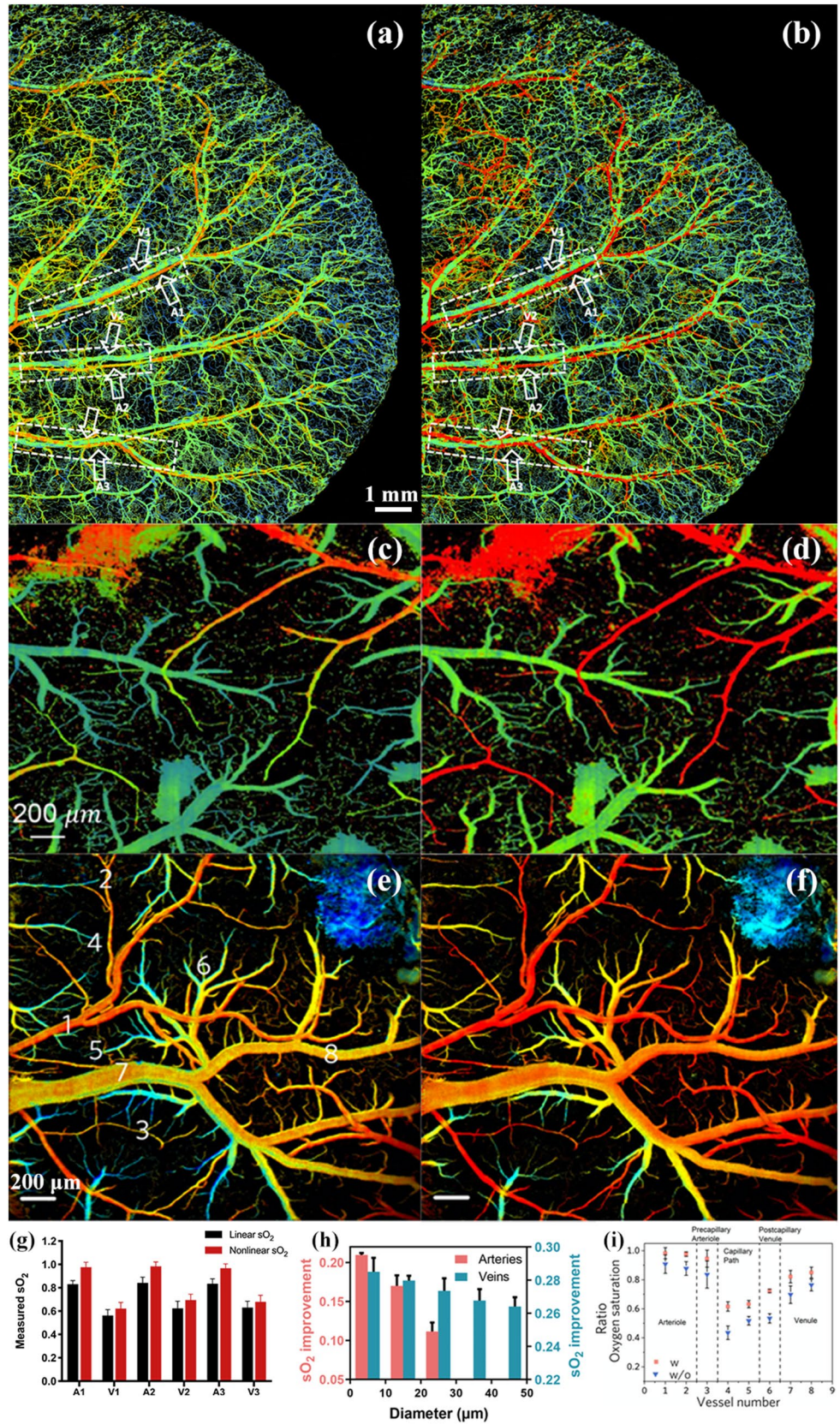
system axial resolution, leading to the result that the collected photoacoustic signals are not entirely from the vessels in the imaging voxel. This compensation method can be more helpful to the situation where the μ_a is high or the imaging system with poor axial resolution.

By using multiple wavelengths to do sO_2 mapping, the wavelength-dependent optical attenuation may be a problem and induce errors, [74, 79]. To solve this, in 2021, Zhu et al. developed a self-compensation method to compensate for the optical attenuation problem, shown in Fig. 4c, d, h [76]. In this work, the results from the Monte Carlo simulation showed that the differences in the focal position, vessel diameter, and imaging depth can reduce ~ 60% in sO_2 calculation. Even for the shallow target which is usually imaged in OR-PAM, the severe and inhomogeneous scattering can cause significant attenuation to local optical fluence, and further induce error to sO_2 measurement. To calibrate for it, a three-wavelength OR-PAM is developed in this work to build up a linearized wavelength-dependent fluence compensation model. In the inhomogeneous tissue where the scattering is dominant, the absorption can be assumed proportionally to the absorption coefficient. Thus, the amplitude of photoacoustic signals from one acoustic voxel can be described as:

$$PA_\lambda = k_0 \Gamma \eta \cdot \int \exp\left(-\frac{2l^2}{r^2}\right) F_\lambda(l) \mu_a^\lambda(l) dl, \tag{14}$$

where k_0 depicts the peak value at the acoustic beam's center and $k_0 \exp\left(-\frac{2l^2}{r^2}\right)$ denotes the acoustic detection sensitivity, r is the characteristic acoustic beam radius, $F_\lambda(l)$ and $\mu_a^\lambda(l)$ are optical fluence and absorption coefficient at position l. Considering the scattering linearity in a narrow wavelength band, the residue of local fluence can be assumed as $F_\lambda = F_{\lambda_0} + F'_{\lambda_0}(\lambda - \lambda_0)$, where F'_{λ_0} represents the gradient index at λ_0. Then Eq. (14) can be rewritten as:

$$PA_\lambda = \mu_a^\lambda \cdot \left[W_1 + W_2(\lambda - \lambda_0)\right]$$

$$W_1 = k_0 \Gamma \eta \cdot \int \exp\left(-\frac{2l^2}{r^2}\right) F_{\lambda_0}(l) dl$$

$$W_2 = k_0 \Gamma \eta \cdot \int \exp\left(-\frac{2l^2}{r^2}\right) F'_{\lambda_0}(l) dl \tag{15}$$

where $\mu_a^\lambda(l)$ is replaced with μ_a^λ when assuming the absorption coefficient is uniform in the target. The new photoacoustic amplitude equation becomes a product of the absorption coefficient and a linear function of wavelength. After combining the Eqs. (1), (15) can be shown as:

$$PA_\lambda = \left[sO_2 \varepsilon_\lambda^{HbO_2} + (1 - sO_2)\varepsilon_\lambda^{HbR}\right] \cdot \left[\overline{W_1} + \overline{W_2}(\lambda - \lambda_0)\right] \tag{16}$$

where $\overline{W_1}$, $\overline{W_2}$ are the product of βC_{Hb} and W_1, W_2, respectively. When the λ and λ_0 are set down, there are three unknowns in this equation: sO_2, $\overline{W_1}$, and $\overline{W_2}$. Thus by selecting three neighboring wavelengths, the sO_2 can be figured out. This work considers the wavelength-dependent optical attenuation problem and uses a self-compensation method to improve the accuracy of the sO_2. Different from the above absorption saturation compensation method which works better for large vessels, this compensation method can be more effective in small and deep vessels.

3.3.2 Acoustic compensation

The photoacoustic signals generation process mainly consists of two parts: optical absorption and acoustic detection. Besides the optical fluence attenuation, the acoustic signals can also be affected by many factors, for instance, the laser pulse width, absorber size, and ultrasound transducer's characters [81]. Thus, besides local fluence, the collected acoustic signals should also be compensated for in concrete circumstances. In 2020, Liang et al. developed an acoustic-spectrum compensation method for OR-PAM to improve the accuracy of sO_2, shown in Fig. 4e, f, i [77]. In this work, the different sizes of blood vessels can lead to nonuniform spectral response via the piezoelectric ultrasonic transducer, which may cause inaccurate measurement of the concentrations of HbO_2 and HbR. The final collected photoacoustic spectrum $A(\omega)$ is the convolutional result of the initial photoacoustic signal $I(\omega)$, the Fourier transformed function of the optical fluence rate $\mathcal{F}(\omega)$, and the transfer function of the imaging system $D(\omega)$ as follows:

$$A(\omega) = \Gamma \cdot D(\omega)\mathcal{F}(\omega)I(\omega), \tag{17}$$

where $\mathcal{F}(\omega)$ is decided by the pulse duration of optical fluence and $D(\omega)$ is determined by the ultrasound transducer. Owing to the spectral product $D(\omega)\mathcal{F}(\omega)$, the spectrum of initial photoacoustic signal $I(\omega)$ is distorted to the spectrum of the final signal $A(\omega)$. To do compensation, the operator $\mathcal{F}^{-1}(\omega)D^{-1}(\omega)$ is precalculated and predetermined to figure out the unaffected signal spectrum. After acquiring the unaffected initial photoacoustic signal $I(\omega)$, the authors used the linear model Eq. (4) to figure out the sO_2. By using this compensation method, the sO_2 mapping accuracy can be improved ~ 15% in mouse brain imaging.

4 Blood flow

Blood flow speed is a critical physiological parameter [21], offering important information for estimating the wall shear rate [82], detecting angiogenesis [83], and diagnosing many diseases including diabetes [84], stroke [85], and

Table 3 Summary of the attributes of photoacoustic flowmetric methods. OE, TC, and, TT are short for optical encoding, target correlation, and thermal tagging photoacoustic flowmetric methods; PH, UH, CWOH, and POH are short for photothermal heating, ultrasonic heating, continuous-wave optical heating, and pulsed optical heating. I is short for whether it can support imaging

Method	Measured flow range	I	Advantages	Shortcomings
Direct [75, 91, 92]	0.04–0.25 mm/s [91]	N	High robustness in spatial domain measurement	Require high scanning speed
OE in temporal domain [93–96]	0.055–8.8 mm/s [93] 3.5–203 mm/s [95]	N	Higher contrast and lower background noise	Measurable flow velocity is limited to the SNR
OE in spatial domain [97, 98]	0.02–1.4 m/s [97] 0.01–25 mm/s [98]	N	Can measure flow in homogeneous media	Cannot provide directional information
TC in temporal domain [99, 99–107]	0.1–12 mm/s [99] 14–200 μm/s [101] 0.15–1.5 m/s [105]	Y	Support imaging sensing; Provide flow direction	Time-consuming for autocorrelation
TC in spatial domain [108, 109]	1.13–13.20 mm/s [108]	N	Detect depth-dependent flow velocity; Not affected by the particle size	Measurement accuracy degraded with increasing flow velocity
TT based on PH [111]	1–21 mm/s [111]	N	Does not require high spatial resolution; high measurement depth	Cannot support the abundant intricated blood vessel
TT based on UH [112–114]	2.97–41 mm/s [112] 0.24–11.8 mm/s [113]	N	Both the heating and the detection have tight acoustic focusing to achieve high resolution	Heating impulse by HIFU can generate lots of heat
TT based on CWOH [115]	11.8–236 mm/s [115]	Y	Single laser source; Heating/detection at the same sides of sample	Heating cycle is time-consuming
TT based on POH [116]	1–23 mm/s [116]	Y	High-speed simultaneous Multifunctional imaging	Cannot provide directional information

Alzheimer's disease [86]. Many conventional imaging methods consisting of optical coherence tomography (OCT) [87], ultrasound (US) [88, 89], and laser speckle contrast imaging (LSCI) [90] can satisfy blood flow imaging, but they all suffer from low contrast to blood, low resolution for cellular insight, and low sensitivity because of the surrounding artifacts. Owing to the high contrast to hemoglobin, subcellular spatial resolution, and enough sensitivity to optical absorption, photoacoustic imaging has drawn growing attention for blood flowmetry recently [64, 91–114]. Table 3 shows the summary of the attributes of various photoacoustic flowmetric methods.
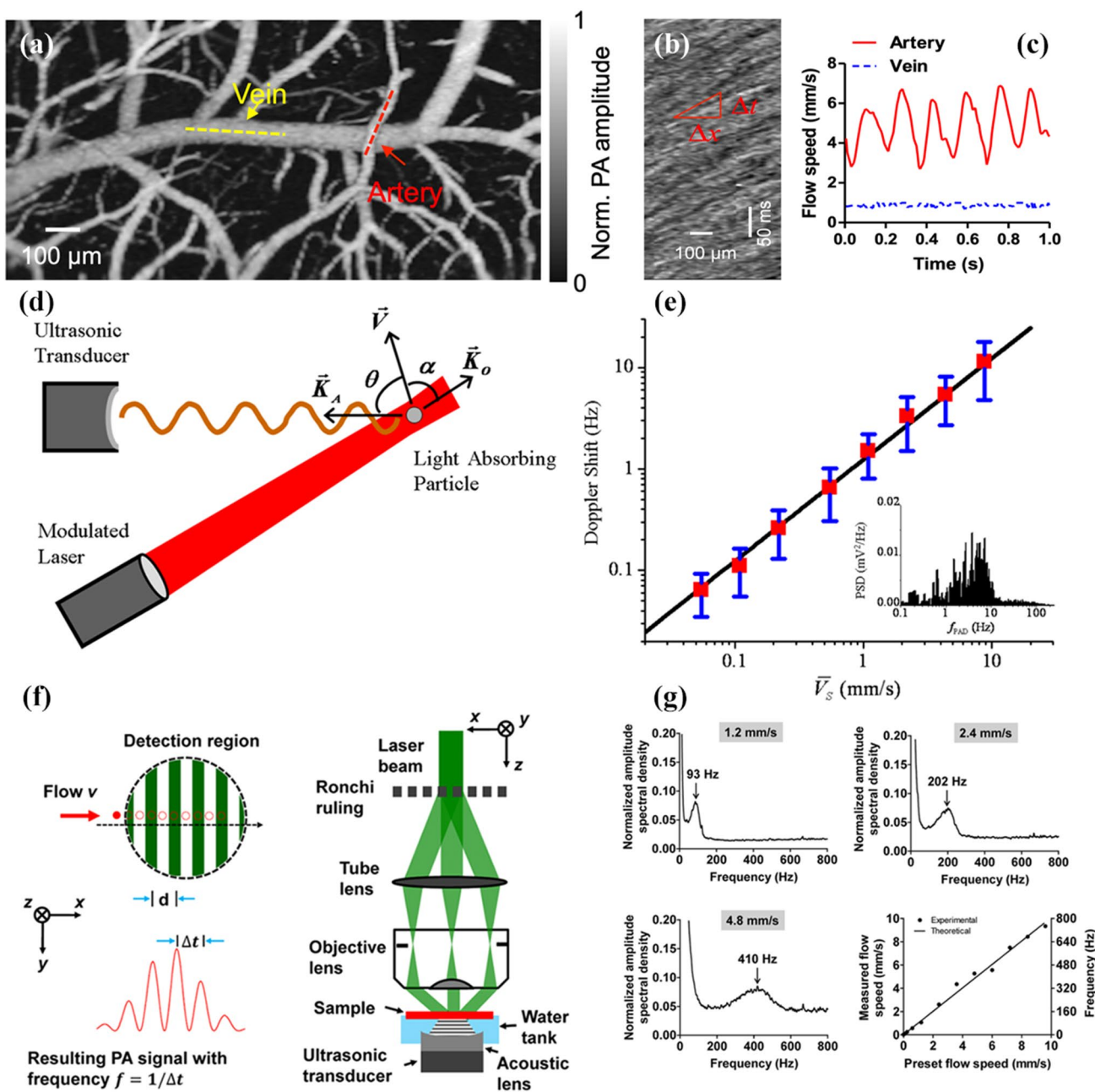
4.1 Direct measurement

Based on the high optical absorption, photoacoustic imaging can be directly used to sense the flow speeds of the sample [75, 91, 92]. In 2011, Wang et al. developed a voice-coil-based fast scanning OR-PAM to measure the flow speeds [91]. In this work, the carbon particles and whole blood in a tube are measured by analyzing the slopes of the streaks generated by the time trajectory path of the target. When the target is flowing with speed v in x axis, the photoacoustic probe is placed to do scanning with speed v_{motor} in x axis. The flow speed distribution along the depth direction of the tube can be acquired based on real-time B-scan images.

According to the real-time B-scan images, the flow velocity distribution along the depth of the tube can be obtained. By plotting the distribution of photoacoustic signal along the x axis at a specific depth z as a function of time, the flow speed at this depth can be figured out based on the slope of each target particle trajectory as:

$$v_a(z) = k\frac{\Delta x}{\Delta t + \frac{\Delta x}{v_s}} = k\frac{1}{1 + \frac{\Delta x/\Delta t}{v_s}}\frac{\Delta x}{\Delta t},$$ (18)

where $v_a(z)$ is the flow speed of target particle in depth z, Δx is the distance displacement in x axis, Δt is the time displacement in t axis, k is the constant factor, v_s is the motor scanning speed. If $v_s \gg v$, Eq. (18) can be approximated as $v_a(z) = k\frac{\Delta x}{\Delta t}$. Thus, by calibrating for k and measuring Δx and Δt in B-scan images, the target flow speed can be figured out. The flow speed is further calculated in the frequency domain for better robustness. The authors later measured the tube-filled whole bovine blood in the range of 0.04 to 0.25 mm/s. Finally, the author measured the single RBCs flowing in the capillaries of the mouse ear. In 2013, the authors developed the single-cell photoacoustic flowoxigraphy and used this method to realize the label-free in vivo imaging of single red blood cells [92]. In 2015, the authors extended this method to measure the cerebral blood flow (CBF) before and during the electrical stimulations for functional brain action studies, shown in Fig. 5a–c [75].

Fig. 5 a–c The blood flow location in the somatosensory area in the right hemisphere of the brain, space–time plot acquired along the vein via scanning, and the measured time traces of the cerebral blood flow speeds by direct measurement [75]. **d–e** The system and flow measurement results based on the modulated continuous-wave laser beam [93]. **f–e** The principle, measured relationship between the preset flow speeds and spectral density, and the comparison between the preset flow speeds and measured flow speeds [98]. All figures are reprinted with permission

4.2 Optical encoding

4.2.1 Optical temporal-domain encoding

In 2007, based on the photoacoustic Doppler effect, Fang et al. used a modulated continuous-wave laser beam to encode the absorber flow into photoacoustic signals, shown

in Fig. 5d–e [93]. The mathematic principle is shown as follows:

$$I(t) = \frac{I_0}{2}\left[1 + \cos\left(2\pi f_0 t\right)\right], \tag{19}$$

where $I(t)$, I_0 are the time-variant and peak light intensity, f_0 is the modulation frequency. Due to the modulated incident

light, the generated photoacoustic signals will also be variable with the frequency f_0 when the target absorber is static. However, when the absorber (e.g. red blood cell) is moving, the frequency of the collected photoacoustic signals will have a Doppler shift, which is related to the moving speed and direction. The flow speed of the absorber can be expressed as:

$$v_a = \frac{f_{shift}}{f_0\left(\frac{\cos\beta}{v_{us}} - \frac{\cos\alpha}{v_{light}}\right)},$$ (20)

where v_a, v_{light}, v_{us} are the speeds for absorber, modulated light, and generated ultrasound, $\cos\alpha$ is the angle between the absorber flow direction and light transmission direction, $\cos\beta$ is the angle between the flow direction and the transducer's view line. Considering the v_{light} is nearly five orders of magnitude larger than v_{us}, the term $\cos\alpha/v_{light}$ in Eq. (20) is negligible. By measuring the f_{shift} and predetermined f_0 and $\cos\beta$, the absorber flow can be figured out. By measuring the set flow velocity for carbon particles in the range of 0.055–8.8 mm/s, the authors validated their method. However, the minimum measurable flow velocity is limited to the system frequency resolution while the maximum measurable flow velocity is limited to the system signal-to-noise ratio. Besides, this method cannot provide directional resolution in depth.

To solve the limitation of measurable velocity and acquire spatial resolution, in 2010, Sheinfeld et al. improved the photoacoustic Doppler method via burst excitation [95]. This method enabled flexible external modulation and highly sensitive heterodyne detection, which relieved the tradeoff between system sensitivity and maximum measurable Doppler shift. Different from modulating the incident continuous-wave laser beam in sinusoidal form, Sheinfeld used rectangularly enveloped sinusoidal bursts to do modulation, the equation can be expressed as:

$$I(t) = \frac{I_0}{2}\left[1 + \cos\left(2\pi f_0 t\right)\right] \sum_i rect\left(\frac{t - iT_r}{T_d}\right),$$ (21)

where T_r, T_d are the pulse repetition interval and pulse duration for i^{th} burst. The condition that T_r is larger than the ratio of the detector-target distance and the light speed should be satisfied to ensure the adequate time for transmitting successive photoacoustic signals. The flow velocity can be calculated via Eq. (20). By involving the tone burst excitation to modulated incident light, this method enables heterodyne detection, which improves both the system sensitivity and maximum measurable flow velocity. Finally, the authors improved the photoacoustic flow velocity measurement range from 3.5 to 203 mm/s.

4.2.2 Optical spatial-domain encoding

Besides time-domain modulation, the structured incident light can also be modulated in the frequency domain. In 2013, Zhang et al. used a spatially modulated incident light to modulate the received photoacoustic signals temporally and further calculate the flow in the homogeneous media [97]. Via generating the fringes in spatially modulated illumination with a pitch of l, the modulation frequency will be $f_0 = v_{us}/l$. Based on Eq. (20), the flow velocity can be calculated. Considering the Doppler angle β equaling to $0°$ in this work, the final f_{shift} can be expressed as $f_0\frac{v_a}{v_{us}}$. Besides the central frequency shift method, the authors also measured the flow in the other three methods based on the arrival time shift, phase change, and temporal scaling. However, compared with the other three methods, the central frequency shift manifests its advantage in measuring the absolute flow speed rather than the relative value. Owing to the higher SNR provided by the pulsed excitation compared with the continuous-wave laser beam, the maximum measurable flow velocity can be increased greatly. Considering the maximum frequency response of the transducer in their system is 105 MHz, the theoretic maximum measurable flow speed will be up to $\sim$3700 m/s. The authors finally demonstrated the phantom experiments with ink in the range of 0.020 m/s to 1.4 m/s.

Conventional optically encoded photoacoustic Doppler flowmetric methods will become less accurate when the Doppler angle is closer to $90°$. Thus, for the superficial imaging method, for instance, the OR-PAM, the above methods cannot measure microvascular flow velocity at shallow tissue accurately where the transverse flow component dominates. To realize transverse flow measurement, in 2014, Yao et al. harnessed the frequency domain modulated structured light to realize the transverse blood flow measurement via OR-PAM, shown in Fig. 5f–g [98]. The particle's transverse flow direction vertical to the structured fringes is defined as the x-axis. When absorbers flow across the light and dark fringes, the acquired photoacoustic signals can be modulated via trains of exciting laser pulses. The structured light excitation I and acoustic detection sensitivity S profile can be expressed as:

$$I(x) =\propto 1 + \alpha\cos\left(2\pi\frac{x}{d}\right)$$

$$S(x) =\propto \exp\left(-\frac{x^2}{2L^2}\right),$$ (22)

where α represents the modulation depth, d denotes the fringe pitch, L indicates the standard deviation of the acoustic detection sensitivity profile. In this work, the axis of the

time interval between two adjacent A-line points is defined as the 'fast time' axis while the axis of pulse repetition interval over trains of laser firings is defined as the "slow time" axis. Then, the amplitude of modulated photoacoustic signals can be expressed as:

$$PA(\tau_s) = \propto \int_{-\infty}^{\infty} I(x)S(x)f(x - v_x \tau_s)dx, \tag{23}$$

where τ_s is the slow time, $f(x)$ is the density distribution of the absorber, and v_x is the x-axis component of the flow velocity v_a. After taking the Fourier transformation, Eq. (23) can be expressed as:

$$\widetilde{PA}(\omega) = \propto \left[\delta(\omega) + \frac{\alpha b}{2} \delta\left(\omega \pm 2\pi \frac{v_x}{d} \right) \right] * \exp\left(-\frac{L^2 \omega^2}{2v_x^2} \right), \tag{24}$$

where $\widetilde{PA}(\omega)$ is the Fourier transform of $PA(\tau_s)$, b is the constant factor needed to be calibrated. Then, the flow speed can be calculated through the peak frequency of the sidebands ω_p as:

$$v_x = \frac{\omega_p d}{2\pi}$$

$$v_a = \frac{v_x}{\cos\gamma}, \tag{25}$$

where γ is the angle between v_x and v_a. Finally, the authors demonstrate the in vivo flow measurement in the mouse ear through OR-PAM. The measured flow speed in a vein is calculated as ~ 1.9 mm/s, which agrees with the normal physiological value.

4.3 Target correlation

4.3.1 Target correlation in the time domain

In optical encoding photoacoustic Doppler flowmetric methods, photon density wave is exploited to calculate frequency shift for flow measurement. However, the target itself can be treated as a moving source, which can also cause a photoacoustic wave frequency shift received by the ultrasonic transducers. In 2010, Yao et al. realized the transverse flow imaging based on photoacoustic Doppler bandwidth broadening of flowing particles, shown in Fig. 6a–c [99]. The factors capable of bandwidth expanding are various including the transit time, Brownian motion, velocity gradient, and turbulence. Compared to the transit time, the others are negligible. Thus, when seeing the target as a moving target, the dominant Doppler bandwidth broadening is caused by two photoacoustic signals' transit time delay received by the edges of the ultrasonic transducer as follows:

$$B_d = f_{L_1} - f_{L_2} = 2f_0 \frac{v_a}{v_{us}} \sin\theta \sin\varphi \approx f_0 \frac{v_a}{v_{us}} \frac{D}{F} \sin\theta$$

$$v_a = \frac{B_d \cdot F \cdot v_{us}}{f_0 \cdot D \cdot \sin\theta}, \tag{26}$$

where v_a, v_{us} are the particle flow velocity and sound speed, θ is the Doppler angle decided by the flow direction and transducer view line and is usually set as 90 degree for maximum Doppler bandwidth, φ is the effective aperture angle of the acoustic lens, f_0, D, and F are the center frequency, the diameter, and the focal length of the ultrasonic transducer, respectively. Then by generating sequential A-scans, the Doppler bandwidth broadening can be calculated as [64, 100]:

$$B_d = \frac{k}{T} \left(1 - \frac{\left| \sum_{i=1}^{n} \tilde{p}_i \tilde{p}_{i+1}^* \right|}{\sum_{i=1}^{n} \tilde{p}_i \tilde{p}_i^*} \right)^{1/2}, \tag{27}$$

where T, n are the time interval and number for sequential A-scans, k is a system constant factor decided by the confocal configuration of OR-PAM, $\tilde{p}_i$ is determined by Hilbert transformation from i th photoacoustic signal p_i. The various particle flow velocities can be corresponding to different Doppler bandwidth broadening B_d. After using the phantom experiments for calibration, the quantitative velocity-bandwidth linear relationship can be determined for further flow imaging. If the image is acquired by motor scanning whose velocity is at the same level of the flowing particle, the true particle velocity should be decomposed from the combination of the flow velocity and the motor scanning velocity. The advantages of this method are not only it doesn't need the entire trace of the particle movement but also it is not sensitive to the particle size. Furthermore, compared to other photoacoustic flowmetric sensing without imaging, this method can realize the velocity imaging with directions. In this work, the authors imaged both sO₂ and blood flow speeds along the main vascular trunks. Finally, the authors used this method to realize a velocity measurement range from 100 μm/s to 12 mm/s. However, this method requires abundant A-lines to do autocorrelation calculation, which consumes much time for imaging of the whole area. What's more, the linear relationship between the flow velocity and bandwidth broadening will become weaker when the flow velocity is higher, which limits the maximum velocity measurement [64].

Another flowmetry method named photoacoustic correlation spectroscopy (PACS) is developed by Chen et al. in 2010 [101], which arises from fluorescence correlation spectroscopy (FCS) [102]. In this method, the light distribution mode is considered to evaluate the autocorrelation condition of flowing particles. When using focused light as excitation,
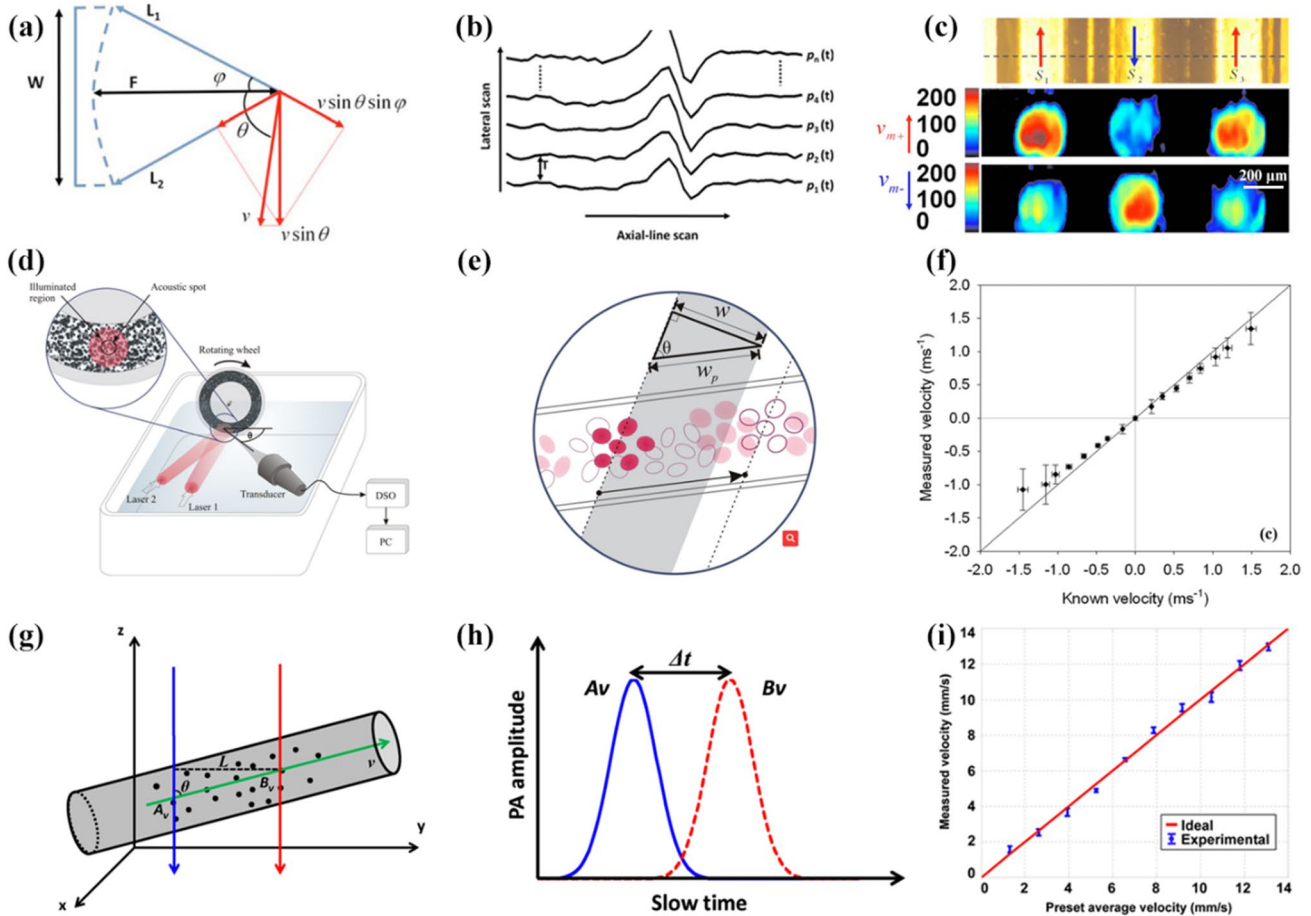
Fig. 6 **a–c** Respectively the probe-beam geometry, sequential A-scans used for calculation, and measured particle flow with different scanning directions from the target correlation photoacoustic Doppler bandwidth broadening flowmetric method [99]. **d–f** Respectively the experimental setup, demonstration of de-correlation within finite transducer beam width, and measured flow results using 3.5 MHz cylindrically focused transducer by the temporal cross-correlation photoacoustic flowmetric method [105]. **g–i** Respectively the principle, shifted time of PA signals from two locations, A_v and B_v, and the comparison of flow results by spatial-domain target correlation photoacoustic flowmetric method [108]. All figures are reprinted with permission

it generates the Gaussian distribution in all directions as $I(x, y, z) = I_0 \exp\left(\frac{-2x^2}{r_0^2} + \frac{-2y^2}{r_0^2} + \frac{-2z^2}{z_0^2}\right)$, where I_0 is the peak intensity, $x(y)$ and z are the beam's radial and axial position, r_0 and z_0 are the radial and axial radii [103]. The flow measurement using the normalized autocorrelation function (ACF) in Gaussian form has been discussed in FCS as follows [104]:

$$G(\tau) = G(0) \times e^{-\left(\frac{\tau}{\tau_0}\right)^2}, \tag{28}$$

where τ is lag time, $G(\tau)$ is the ACF, $G(0)$ is a constant factor related to the particle density in the probe region, τ_0 equals to $\frac{r_0}{v_a}$, v_a is the flow velocity of the absorber and can be expressed from Eq. (28) as:

$$v_a = \frac{r_0 \cdot \sqrt[2]{\ln\left[\frac{G(0)}{G(\tau)}\right]}}{\tau}, \tag{29}$$

This method is based on the assumption that incident light is in Gaussian form, making it a suitable flow measuring tool for the optically focused imaging system, for instance, the OR-PAM. In 2015, based on this flowmetric method, Ning et al. realized the simultaneous imaging of for C_{Hb}, sO_2, and BF through OR-PAM [73]. However, they used 100 A-lines with a 100-μs interval for flow decorrelation analysis, which is still time-consuming for a large field of view (FOV), making it difficult for real-time imaging.

In 2012, Brunker et al. used the temporal cross-correlation method that arose from time correlation ultrasound flowmetry to demonstrate the photoacoustic Doppler flowmetry approach, shown in Fig. 6d–f [105]. In this

method, two laser pulses with time delay T are excited to generate two photoacoustic signals [106, 107]. The waveform of these two photoacoustic signals are the same in shape but temporally shifted with each other because of the red blood cell (RBC) cluster flowing. Based on the cross-correlation of these waveforms, the temporal shift can be calculated as $t_s = l\cos\theta/v_{us}$, where l is the particle moving distance, θ is the Doppler angle, v_{us} is the speed of ultrasound. Considering the particle flow velocity v_a equaling to l/T, then v_a can be expressed as:

$$v_a = \frac{v_{us} \cdot t_s}{T \cdot \cos\theta},\tag{30}$$

By measuring the time shift t_s of two photoacoustic signals, the particle flow velocity v_a can be calculated. This method requires the moving particle neither totally moving out of the transducer's focal zone nor changing significantly in its geometry or density at time interval T. Finally, via a tissue phantom similar to RBCs, the authors demonstrated the measurement of flow velocity. Finally, the flow speed in the range of 0.15 to 1.5 m/s is quantified with accuracy as low as 1%. However, the precision of this method relies on the accuracy of time-shift measurement, which can be affected by the laser pulse energy fluctuations, the time jitter in the system synchronization, and the spurious absorbers moving in the water.

4.3.2 Target correlation in time spatial domain

To overcome these limitations, In 2013, Liang et al. developed a spatial cross-correlation photoacoustic flowmetric method based on a digital micromirror device (DMD), shown in Fig. 6g–i [108]. In this method, a pair of spatially resolved laser beams are generated by DMD with distance l and delay interval t_p and delivered to the moving target so that the speed and the direction of transverse flow can be directly retrieved by cross-correlated photoacoustic signals. Then the time shift Δt between the photoacoustic profiles at these two focal points can be used to calculate the particle flowing velocity as:

$$v_a = \frac{L}{(t_p + \Delta t) \cdot \sin\theta},\tag{31}$$

where θ is the flow-detector angle. Finally, the authors demonstrated the flow measurement in a range of 1.13–13.20 mm/s using the absorbing particles covered by chicken tissue. Owing to the spatial cross-correlation, this method can not only detect the flow velocity encoded with depth but also get rid of the effect from particle size. However, the flow measurement can become inaccurate when flow velocity increases. In their future work [109], the

spatial cross-correlation flow measurement was conducted on the mouser ear to estimate the in vivo blood flow.

4.4 Thermal tagging

### 4.4.1 Thermal tagging based on photothermal heating

Conventional photoacoustic Doppler flowmetric methods not only require the light beam to be subcellular size but also require heterogeneity of the moving particle. This limits the imaging depth and influences the Doppler effect. Inspired from thermal diffusion flowmetry (TDF) [110] which is commonly used for flow measurement, Sheinfeld et al. developed a thermal-clearance-based photoacoustic flowmetric method, shown in Fig. 7a–c [111]. The principle of this method is that the flowing target can cause thermal diffusion in surroundings, while the former can be reversely figured out based on the latter. Considering a common situation that blood flows in vessels covered by tissue, the dominant thermal diffusion happens from the heat conduction and convection. By involving the photothermal to induce heat, the heat transfer function can be expressed as:

$$\frac{\partial T(\vec{r}, t)}{\partial t} = \nabla \cdot \left[\alpha(\vec{r})\nabla T(\vec{r}, t)\right] - v(\vec{r}) \cdot \nabla T(\vec{r}, t),\tag{32}$$

where $\vec{r}$ is the spatial coordinates in the heated volume, $T(\vec{r}, t)$ is the local temperature variation along with the time t compared with the baseline temperature T_0, $\alpha(\vec{r})$ represents the thermal diffusivity, $v(\vec{r})$ is the flowing speed. In this work, two optical beams from laser diodes were modulated into a sinusoidal wave in different frequencies: one is used to generate photoacoustic signals, and the other is used to heat the medium and increase its Grueneisen parameter, and further encode the photoacoustic signals. Then its modulation frequency response can be expressed as:

$$F(\omega) = F(0)\frac{t_{eff}}{1 + j\omega t_{eff}},\tag{33}$$

where ω equals to $2\pi f_{PT}$, f_{PT} is the photothermal modulation frequency, $F(0)$ is modulation frequency at baseline temperature, $t_{eff} = (t_{cd}^{-1} + t_{cv}^{-1})^{-1}$, t_{cd} and t_{cv} are time constants for conduction and flow-related convection, respectively. Via fitting $F(\omega)$, the flow v can be estimated from t_{eff}. The authors finally measured the blood flows in a range of 1 to 21 mm/s. Based on thermal clearance, this method doesn't require a system with high spatial resolution and can be used for photoacoustic flow sensing in deeper tissue compared with the conventional photoacoustic Doppler method. However, the method in this work is focused on a single vessel, thus the method needs to be improved for abundant intricated blood vessels.
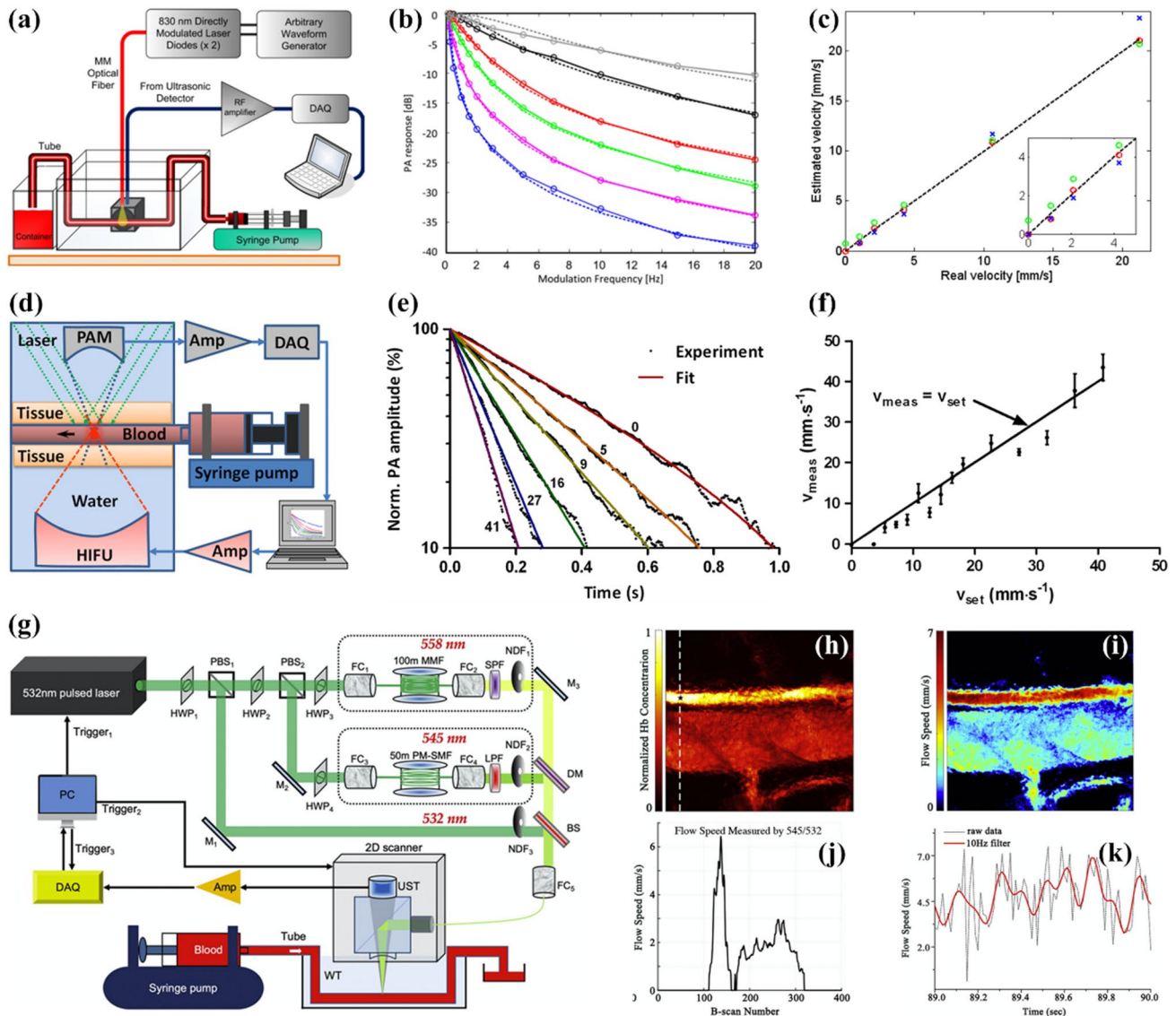
Fig. 7 a–c Respectively the system setup, normalized photoacoustic modulation frequency responses with different flow speeds (1.06 (pink), 2.1 (green), 4.2 (red), 10.6 (black) and 21.2 (gray) mm/s), and the flow measurement results compared with the preset values by the photothermal-thermal-tagging photoacoustic flowmetric method [111]. **d–f** are respectively the system setup, thermal decay curves acquired with different blood flow speeds, and measured flow speed versus set flow speed through the ultrasound-thermal-tagging photoacoustic flowmetric method [112]. **g–k** The system setup, vessel structure, blood flow, speed profiles along with the dashed white line in (h), time-domain blood flow speed in the artery from the pulsed-laserbeam-thermal-tagging photoacoustic flowmetric method [116]. All figures are reprinted with permission. (Color figure online)

4.4.2 Thermal tagging based on ultrasonic heating

Although the photothermal-based thermal-tagging flowmetry can increase the flow sensing depth, the measurement depth is still limited due to the light scattering for photothermal. In 2013, Wang et al. extended this method using the high-intensity focused ultrasound (HIFU) to induce heat for photoacoustic flowmetry, shown in Fig. 7d–f [112]. The authors defined the weighted average temperature in the measured volume of a target as $\tilde{T}(t) = \oint_{\Omega} w_1(\vec{r})T(\vec{r},t)dV$,

where $w_1(\vec{r})$ is the weight factor, Ω is the measured volume. Then, base on Eq. (32), the $\tilde{T}(t)$ can be expressed as:

$$\tilde{T}(t) = \tilde{T}(t_0)e^{-(\tau_{cd}+k_{cv}v_a)t}, \tag{34}$$

where $\tilde{T}(t_0)$ is the weighted average temperature at the initial time, τ_{cd} and k_{cv} are the system constant factor related with conduction and convection, respectively, v_a is the particle flow speed. The altering $\tilde{T}(t)$ can change the

temperature-dependent Grueneisen parameter Γ, and further encodes photoacoustic signals as:

$$\tilde{P}(t) = c_1 + c_2 e^{-(\tau_{cd} + k_{cv} v_a)t}$$

$$v_a = \frac{\frac{1}{t}\ln\left[\frac{c_2}{\tilde{P}(t) - c_1}\right] - \tau_{cd}}{k_{cv}}, \tag{35}$$

where c_1, c_2 are the constant. Via phantom experiments with various blood flow speeds, the system constant factors can be calibrated. Then, the unknown particle flow speed can be determined by the corresponding measured photoacoustic signals amplitudes. Finally, the authors conducted in vitro experiments and measured the blood flow with a range of 2.97–41 mm/s under 1.5-mm-thick tissue. However, the flow direction is not measured in this work. Another problem is the safety problem caused by HIFU heating impulse, which can generate instantaneous heat.

To ensure safety, the authors further used modulated continuous HIFU heating to measure the flow speed [113]. The temperature of the flowing particle in response to sinusoidal heating can be expressed as:

$$T'(t, x) = A_T(x) \sin\left[2\pi f_0\left(t - t_0 - \frac{x}{v_a \cos\theta}\right)\right], \tag{36}$$

where v_a is particle flow speed, $T'(t, x)$ is the temperature variation from baseline, $A_T(x) = A_T(0) \times \exp\left[-\left(\frac{\alpha\beta}{v_a \cos\theta}\right)x\right]$ is the amplitude of temperature variation at x, $x = 0$ is the heating place, α is the thermal diffusivity, β is a constant factor, f_0 is the sinusoidal heating frequency, θ is the angle between the flow direction and x axis. The varied temperature can change the Grueneisen parameter and further modulate the photoacoustic signals. Then, the relationship between the carrier photoacoustic signal's Doppler shift and the flow speed can be expressed as:

$$v_a = -\frac{v_m}{\Delta f \cos\theta} f_0, \tag{37}$$

where v_m is the scanning speed along the flow direction. Finally, the authors achieved the lowest and highest detectable flow speed at 0.24 mm/s and 11.8 mm/s, respectively. Owing to the sinusoidal heating, the maximum photoacoustic amplitude change and temperature fluctuation were controlled to $\pm 6.2\%$ and ± 1.3, respectively, which is safe enough for in vivo imaging.

Based on a similar principle, Zhang et al. developed an optical modulated thermal tagging method to acquire flow speed in 2014 [114]. In this work, the local temperature was modulated by a sinusoidal heating beam, and further, encode the photoacoustic signals. The flow speed v_a can be also estimated from Eq. (37). When $v_m \gg v_a \cos\theta$ and $\theta = 0^\circ$,

by taking photoacoustic signals at positions x_1 and x_2 with $\Delta x = x_2 - x_1$ and time delay Δt, the flow speed v_a can be simplified as $\Delta x/\Delta t$. This method can ensure both the photothermal encoding and the photoacoustic detection periods use the endogenous optical absorption contrasts. However, the heating and detection beams are on the opposite sides of the sample, limiting the sample thickness and absorbance.

4.4.3 Thermal tagging based on optical heating

To ensure the heating/detection period at the same side, Liu et al. developed a single-light-source-based photoacoustic flowmetry via OR-PAM [115]. Different from using diffused light or focused ultrasound for heating, the authors used the focused laser beam for both photothermal heating and photoacoustic detection, which simplifies the system configuration for future in vivo applications. In each heating cycle, 500 laser pulses with a 10 kHz repetition rate are used to heat the flowing medium. The mathematical model is similar to Eq. (35) as:
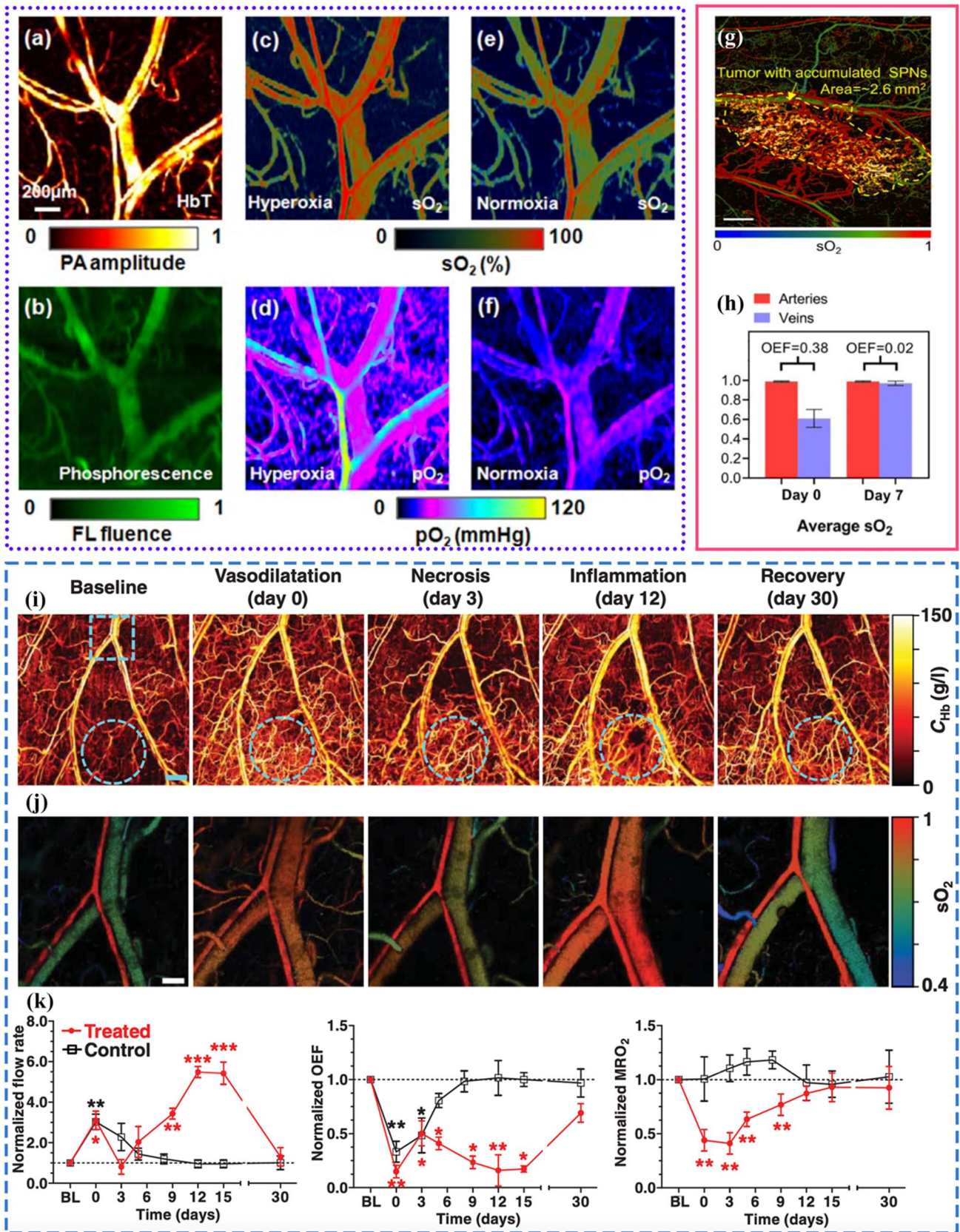
$$\tilde{P}(t) = Ae^{-(\alpha + k v_a)t} + B, \tag{38}$$

where A, B, α, k are system constant factors that need to be calibrated. By employing phantom experiments via different sample flowing speeds, these constant factors can be used for in vivo flow measurement. Finally, the authors realized the flowing blood phantoms at speeds from 11.8 to 236 mm/s and measured in vivo blood flow speeds in the microvasculature in the mouse ear. This method only harnesses a single laser source for both heating and detection periods, which simplifies the system setup for reflection-mode OR-PAM. However, the time interval between each heating cycle is ~ 100 ms, making it difficult for fast flow measurement.

To realize high-speed multi-contrast OR-PAM, Liu et al. developed a fast thermal-tagging-based dual-pulse flowmetric method with A-line speed, shown in Fig. 7g–k [116]. This method enables simultaneous imaging of C_{Hb}, sO_2 and BF under single scanning. The principle is that when two successive pulses are shone onto the targets, the heat generated by the first pulse can elevate the local Grueneisen parameter and further increase the photoacoustic amplitudes induced by the second pulse. The local Grueneisen parameter is a function of the particle flow speeds. Thus, by reversely measuring the increment amplitude of second photoacoustic signals, the flow speeds can be figured out as:

$$PA_1 = k\eta\Gamma_0 F_1 \mu_{a1}$$

$$PA_2 = k\eta(\Gamma_0 + \Delta\Gamma)F_2\mu_{a2}$$

$$\Delta\Gamma = aF_1\mu_{a1}e^{-(\tau_\alpha + b v_a)\delta t}, \tag{39}$$

where PA_1, PA_2 and F_1, F_2, and μ_{a1}, μ_{a2} are the photoacoustic amplitudes, optical influence, and absorption coefficients for the first and second pulses, respectively; Γ_0, $\Delta\Gamma$ are the baseline and increment value of Grueneisen parameter; a, τ_α, b are system constant factors; δt is the dual-pulse time interval. Then, the PA_2 can be rewritten as:

$$PA_2 = \frac{F_2\mu_{a2}}{F_1\mu_{a1}}PA_1 + \frac{F_2\mu_{a2}}{F_1\mu_{a1}}PA_1^2 \cdot M \cdot e^{-(\tau_\alpha+bv_a)\delta t}$$

$$v_a = \frac{\frac{1}{\delta t}\ln\left[\frac{\frac{F_2\mu_{a2}}{F_1\mu_{a1}}PA_1^2 \cdot M}{PA_2 - \frac{F_2\mu_{a2}}{F_1\mu_{a1}}PA_1}\right] - \tau_\alpha}{b}, \tag{40}$$

where $M = \frac{a}{k\eta\Gamma_0^2}$. M, τ_α, b are system constant factors that can be fitted by conducting the phantom experiments. The photoacoustic amplitudes of two successive pulses can be used to decide the flow speed directly. The dual-pulse flowmetric method enables fast flow measurement at sub- microsecond level. Finally, the authors demonstrated the simultaneous wide-field multi-functional OR-PAM in the mouse ear. This method significantly reduces the flow measurement time from tens milli-seconds to sub-microseconds, which can enable fast multi-functional OR-PAM. This method requires high laser source performance for low pulse-to-pulse energy fluctuation of two laser pulses. In this work, the fiber SRS effect is used to generate multiple laser pulses from one seed pulse, resulting in low pulse-to-pulse energy fluctuation.

5 Partial oxygen pressure

PO_2, or oxygen tension is a significant physiological value indicating the balance between local oxygen delivery and consumption in blood vessels [117, 118]. Both sO_2 and pO_2 are important for oxygen metabolism analysis in blood imaging. The relationship of sO_2 and pO_2 can reflect the hemoglobin binding affinity of oxygenation [119]. Compared with the sO_2, pO_2 is more suitable for solid tumor study, where the blood vessels are in tortuosity and necrosis period limiting the oxygen transportation [120].

5.1 Photoacoustic lifetime imaging (PALI)

Owing to the high optical absorption of hemoglobin, photoacoustic imaging can provide high contrast for pO_2 measurement [51, 66, 121–128]. Similar to other optical methods, photoacoustic pO_2 sensing is also based on measuring the lifetime of oxygen-sensitive dye from the excited state to the ground state [129, 130]. The first photoacoustic lifetime imaging (PALI) was developed by Shai Ashkenazi et al. in 2010 [121], shown in Fig. 8a–f. In this work, the methylene blue (MB) is used as an oxygen-sensitive dye to acquire deep pO_2 measurement because the absorption peak of MB is at ~ 660 nm where the tissue optical absorption is relatively low. For their system setup, two laser sources are used for pumping the dye-labeled molecules and probing the transient absorption period, respectively. The detected photoacoustic signals PA are the function of the time interval τ between the pump and probe pulses as:

$$PA = PA_0e^{-\frac{\tau}{T}}, \tag{41}$$

where PA_0 is the initial transient photoacoustic amplitude, T is the lifetime. By using trains of different pump-probe delays to do exponential fitting, the lifetime T can be extracted. Based on the Stern–Volmer relationship, pO_2 can be calculated from already known lifetime T [122] as:

$$pO_2 = \frac{T^{-1} - T_0^{-1}}{k}, \tag{42}$$

where T_0 is the lifetime without oxygen, k is quenching rate constant. The constants T_0 and k for various dyes have been examined and published in the literature [131, 132]. For instance, for MB used in this work, $T_0 = 79.5\mu s$ and $k = 0.0036\ \mu s^{-1}\ mmHg^{-1}$. By tuning the probing laser wavelength to 810 nm, the authors conducted the phantom experiments through two independent plastic tubes filled with the MB dye solution with different oxygen levels. The resulted sufficient contrast offered by photoacoustic imaging signifies that the absorption at the excited state can be more than 4 times higher than that at the ground state. The authors successively measured pO_2 in the range of 0.4 to 153 mmHg with a low standard deviation. However, during pO_2 quantitative imaging, the authors observed significant deviations from the set values and obvious scattering due to the fluctuated pulsed energy for both pump and probe laser sources. The authors demonstrate the potential of PALI for clinical study combined with photodynamic therapy (PDT) for real-time therapy monitoring. In their future work, they combined PALI with normal ultrasound and photoacoustic sensing for more contrast imaging, demonstrated pO_2 imaging via tumor hypoxia model in small animals [122], and monitored tissue oxygen changes induced by different

external modulations including controlling the percentage of the oxygen inhaled by mouse and performing acute ischemia model [123].

5.2 *Multi-modality pO$_2$ imaging*

To study the relationship of pO$_2$ and sO$_2$ in vivo, Wang et al. integrated the OR-PAM and fluorescence confocal microscopy (FCM) to realize the dual-modality functional microscopy [66]. In the setup, a 523-nm pulsed laser is used as a pump for both exciting the oxygen-sensitive phosphorescent probe (Pd-meso-tetra porphyrin) and pumping a dye laser with tunable wavelengths (560–590 nm). The dye laser is used for hemodynamic imaging. The generated photoacoustic and phosphorescence signals are collected by ultrasound transducer (US) and a photomultiplier tube (PMT), respectively. By tuning the wavelength to 570 and 578 nm, sO$_2$ mapping can be obtained by linear spectral unmixing method. The pO$_2$ in the same image region can be estimated by measured phosphorescence lifetime based on Eq. (42). To investigate how one of pO$_2$ and sO$_2$ can affect the other, the authors modulate the mouse's status from hyperoxia to normoxia by changing the inhalation gas from pure oxygen to air. The results first showed that the higher-sO$_2$ area measured by OR-PAM matches well with the higher-pO$_2$ area acquired by FCM. Second, both pO$_2$ and sO$_2$ decreased when the status switched from hyperoxia to normoxia, but the decreasing amplitude is different in arteries and veins. From hyperoxia to normoxia status, the resulting sO$_2$ and pO$_2$ in the arteries decreased differently, while in comparison, both sO$_2$ and pO$_2$ in the veins decreased small, matching well with the nonlinear tendency of oxygen-hemoglobin binding. Finally, the authors built up a dual-modality microscopy system combining OR-PAM and FCM to realize in vivo subcellular imaging analysis of the relationship between sO$_2$ and pO$_2$, making it a potential tool for quantitative analysis of in vivo microenvironmental oxygen transport.

6 Oxygen extraction fraction

OEF is generally considered to be an indicator reflecting the ability of tissue to take oxygen from the surrounding bloodstream in order to maintain the integrity of function and morphology [133]. OEF manifests the oxygen utilization efficiency by the tissue, being an indicator for the diseased models related to hemodynamics, for instance, tumor growth [67] and cerebral ischemia [134]. Typically, the OEF in the ROI can be calculated by measuring the oxygen saturation

average in all surrounding feeding arteries and draining veins as [67]

$$OEF = \frac{sO_{2_f} - sO_{2_d}}{sO_{2_f}}, \tag{43}$$

where sO_{2_f} and sO_{2_d} are the averaged oxygen saturation in all feeding arteries and all draining veins, respectively. Owing to the high sensitivity to hemodynamics, photoacoustic imaging can be a powerful tool for measuring the OEF in different biomedical applications.

6.1 OEF used in ischemic stroke evaluation

OEF is often used as a factor for normality evaluation in brain-related diseased models. Compared with other conventional hemodynamic parameters, e.g., the CBF, OEF is more suitable for evaluating brain status in the ROI. Because CBF mapping of the gray and white matter in the brain can show significant boundary, on the contrary, the OEF mapping shows relatively consistent across the entire brain, which brings a more robust quantitative measurement of OEF in the ROI. Among various brain-related diseases, ischemic stroke is prone when the supply of blood and oxygen is not enough for normal brain hemodynamic activities, which usually arises from thrombosis in the cerebral aorta. Ischemic stroke can cause serious and irreversible diseases like paralysis, communication difficulties, or a visual impairment, thus the study of ischemic stroke's pathogenesis is important. In 2011, Hu et al. demonstrated ischemic stroke under longitudinal monitoring via OR-PAM [134]. In this work, an ischemic stroke model is made on mice by performing the middle cerebral artery occlusion (MCAO) and OEF is extracted from the averaged sO$_2$ values in the middle cerebral artery (MCA) and draining veins. The authors found during the MCAO, the OEF in the stroke region elevated significantly from baseline 0.15 to 0.48 to compensate for the reduced CBF and after MCA reperfusion, the OEF gradually reduced and finally dropped to zero after 24 days, reflecting the brain necrosis. Taking advantage of OR-PAM, the ischemic stroke process can be monitored longitudinally through the intact skull and evaluated quantitatively by OEF measurement. In their future work, based on these disease models, the authors validated the neuroprotection ability of sphingosine 1-phosphate (S1P) against ischemic stroke [135]. The recovery of OEF in the stroke region after treatment manifests the drug's effectiveness.

6.2 OEF used in tumor growth evaluation

Besides cerebral study, OEF is also a good indicator for evaluating tumor growth. Compared with normal tissue, OEF

in tumor tissue is generally poor, indicating the incomplete extraction of oxygen from the blood to tumors. In 2020, Chen et al. developed a dual-wavelength confocal visible/NIR OR-PAM to realize a subcellular insight for observing tumor growth at an early stage, shown in Fig. 8g–h [67]. The authors cultured tumor cells on the mouse ear. After a week's development, the angiogenesis and hypermetabolism in the tumor region become obvious via the combination of visible and NIR OR-PAM. The authors measured the average oxygen saturation in all feeding arteries and all draining veins around the tumor region and calculate the OEF. The resulting OEF shows a significant decrease from 0.38 to 0.02 after 7 days' development of the tumor, indicating the low oxygen consumption in the tumor tissue. The authors finally realized the simultaneous functional and morphologic microvascular tumor imaging including the hemoglobin concentration, oxygen saturation, labeled tumor, vessel diameter, vessel tortuosity, and vessel density. The comprehensive multi-parameter subcellular OR-PAM can provide multiple angles for studying the evolution mechanism in the tumor microenvironment.

Due to the high sensitivity to oxygenation variation, OEF can be used as the indicator to evaluate multiple diseased models including the blast traumatic brain injury [136], diabetes [137], hypercapnia [138], obesity [139], etc.

7 Metabolic rate of oxygen

MRO_2 can directly mirror the oxygen depletion condition in the targeted tissue. It can be used not only for monitoring tissue's healthy status [65, 140], but also for evaluating the effectiveness of treatment [141]. For calculating MRO_2 in ROI, OEF and amount of BF passing through the tissue in ml/100 g/min in the target region should be obtained [142]:

$$MRO_2 = OEF \times BF \times C_\alpha, \tag{44}$$

where C_α is a constant, representing the oxygen molecules capacity per unit volume of blood. In biomedical imaging, MRO_2 is wildly used to evaluate the brain hemodynamic function [142] and observe the hypermetabolism in tumor growth [143].

7.1 Cerebral metabolic rate of oxygen

In the brain-related study, the cerebral metabolic rate of oxygen ($CMRO_2$) is considered as a direct evaluation indicator for neuron activity, energy homeostasis, and brain health. Many brain-related diseased models have been explored by photoacoustic imaging based on $CMRO_2$ analysis [136, 138, 139, 142, 144, 145]. In 2018, Ni et al. combined PACT and magnetic resonance imaging (MRI) to study the $CMRO_2$

mechanism in Alzheimer's disease (AD), which is a common brain disease affecting patients' memory, mind, and behavior [144]. Recent research has revealed obvious features like hypoperfusion and capillary dysfunction in the AD model, however, the relationships to oxygen transport and metabolism in the AD model are still unknown. Due to the high optical absorption and low ultrasonic scattering, photoacoustic imaging can provide high contrast vascular imaging for the mechanism study of AD deep brain tissue. The authors used AD mice to estimate OEF and $CMRO_2$ in mouse brain by PAT and measure the cerebral blood flow (CBF) by perfusion MRI. Finally, the authors found obvious decreased cortical CBF and $CMRO_2$ in aged AD mice compared with the wild-type littermates. The measured $CMRO_2$ are 1.81 ± 0.64, 2.7 ± 0.8, and 2.8 ± 0.67, respectively for 24-month normal mice, 6-month AD mice, and 24-month AD mice, while the detected cortical CBF decreased 30% in 24-month AD mice compared with the age-matched normal mice. The authors ultimately attributed the significant decrease in $CMRO_2$ to the inability of the vascular system to compensate for the decreased oxygen delivery by increasing OEF, which may make the tissue under the condition of hypoxic pressure. Blast traumatic brain injury (bTBI) is also a common brain disease caused by blast shockwave, especially in combat-related injuries. To analyze the dysfunctions mechanism in cerebral microvasculature, Cao et al. developed multi-parametric photoacoustic microscopy to monitor the cerebral hemodynamics and metabolism within four hours after injury [136]. The authors first measured globe oxygen-metabolic responses to blast exposure. The results showed that except for a slight increment of venous sO_2 and blood flow in the blast-exposed group, other functional parameters including the hemoglobin concentration, average arterial sO_2, OEF, CBF, and $CMRO_2$ showed no significant difference in blast-exposed and normal groups. To further examine the relationship between the blast-induced functional variations and vessel types, the authors conducted a single-vessel analysis by sorting out the blood vessels into four types. The results showed that blast-induced sO_2 and blood flow changes are primarily in small veins, and in both large veins and large arteries, respectively. The authors owe the stability of $CMRO_2$ in the blast-exposed model to the firm coupling of increased CBF and reduced OEF. Based on the $CMRO_2$ sensing provided by photoacoustic imaging, the authors afforded a comprehensive understanding of the bTBI mechanisms. The authors further uncovered the $CMRO_2$ change mechanism by photoacoustic imaging in multiple diseased models including the anesthesia effect on the brain [145], hypercapnia [138], and obesity [139].

7.2 Hypermetabolism in tumor growth

Angiogenesis and hypermetabolism are two hallmarks in the tumor developing period, which are highly related to the MRO_2. When a tumor develops, the cancer cells derive nutrients and energy from surrounding feeding vessels to grow and spread, which alters the MRO_2 in local microvasculature. The most obvious change after the early cancer stage is the hypoxia caused by hypermetabolism and restricted blood supply. In 2011, Yao et al. observed the MRO_2 variation at early stage when cancer grows [143]. After culturing B16 melanoma cells on the mouse ear after a week, the vessel is dilated with increased volumetric blood flow rate, ensuring adequate nutrients and oxygen supply for tumor growth and metastasis. Finally, the MRO_2 has a 36% increment. It signifies that melanoma can cause hypermetabolism to tissue at early stage of tumor. After two weeks, the MRO_2 continuously dropped indicating the growing tumor's status changing from hyperoxia to hypoxia. The authors explained two reasons for this: the first reason is the behavior change of tumor from aerobic respiration to anaerobic respiration for pillaging oxygen in fast growth; the second reason is the necrosis in the core area of the tumor, which doesn't consume oxygen but increases tumor weight and reduces the MRO_2. For better demonstration, the authors chose the more transparent U87 human glioblastoma to measure the variation of MRO_2 with tumor growth. After 7 days' development, the oxygen saturation in draining veins was elevated which reflects the hyperoxia at the early cancer stage. Compared with melanoma, glioblastoma expressed a 100% increment in MRO_2, indicating stronger hypermetabolism. By analyzing MRO_2 quantitatively via OR-PAM, the authors demonstrated the hyperoxia phenomenon, indicating the hypoxia-based diagnosis may not be suitable for early-stage cancer. The work also monitored the hemodynamic response and MRO_2 change during hyperthermia therapy and cryotherapy shown in Fig. 8i–k, which are common clinical treatments for cancer.

8 Conclusion and outlook

Photoacoustic imaging is a powerful imaging tool for monitoring hemodynamics not only because of its high contrast based on optical absorption but also due to its ability for multi-functional imaging. This paper summarizes the mainstream methods based on photoacoustic imaging to acquire multi-functional information including C_{Hb}, sO_2, BF, pO_2, OEF, and MRO_2, which are all important indicators for vascular health. The C_{Hb} can be normalized by selecting isosbestic wavelengths which have similar absorption coefficients for oxygenated hemoglobin and deoxygenated hemoglobin. The sO_2 can be mainly acquired linearly and nonlinearly. The linear sO_2 method arises from the spectral unmixing while the nonlinear sO_2 method is based on the saturation from intensity or picosecond/nanosecond pulse width. For more accurate sO_2 measurement, the optical and acoustic compensation methods are introduced aimed at different situations. Photoacoustic flowmetric methods are mainly based on optical encoding, target correlation, and thermal tagging, which encode the modulated light intensity, target density, and heat transit time into the blood flow, respectively. The blood flow can be extracted from the affected photoacoustic signals. The pO_2 is highly related to sO_2 and can be figured out by measuring the lifetime of the oxygen-sensitive dye. OEF and MRO_2 are important indicators directly reflecting the hemodynamic activities and creature vitality and can be calculated by the combination of sO_2, BF, and vessels' structural information. OEF and MRO_2 are wildly used in multiple biomedical applications including the analysis of brain-related diseased models and studies on cancer research. This work detailly introduces the various photoacoustic-based methods to calculate the multiple functional information, benefiting the multi-functional photoacoustic applications in the future.

Nowadays, limited by the alternative commercial laser sources and calculation methods, most photoacoustic imaging based biomedical applications can only obtain one or two functional parameters through single scanning, limiting the potential of simultaneous multi-functional photoacoustic imaging. In the future, two solutions can be taken into consideration for better multi-functional sensing. One way is to update the laser sources which can provide multiple stable wavelengths with sufficient pulsed energy for multi-contrast imaging. The existing similar methods are using SRS-based fiber laser and OPO (Optical parametric oscillator) laser source. However, the former one is limited to the energy and wavelength choice while the latter one is limited to the beam quality and pulse-to-pulse stability. The other way is to improve the functional quantitative methods. For instance, the photoacoustic Doppler bandwidth broadening flowmetry needs multiple times scanning at the same imaging region to acquire blood flow, which is time-consuming and cannot support simultaneous imaging with other functional parameters. Thus, to realize simultaneous multi-functional photoacoustic imaging, better laser sources and improved functional quantitative methods are indispensable. For the preclinical and clinical applications, photoacoustic microscopy (e.g., OR-PAM) can provide high-resolved and multi-contrast molecular imaging, making it powerful tool for tumor metastasis study and brain activity research, which benefits the life science. However, the imaging penetration depth is still a challenge for microscopic imaging tool, limiting its clinical potentials in deeper tissue. In future, one solution is

to alleviate the optical scattering, for instance, using the wavefront shaping method to refocus the scattered photon; the other way is to combine the tomography (e.g., PACT) to realize the multiscale imaging: OR-PAM is used to provide the high-resolved superficial imaging while PACT is used to provide the deep tissue information.

Declarations

Conflict of interest The authors have no conflicts of interest to declare.

Ethical approval This article does not contain studies with human participants or animals.

References

1. Dunn AK, Devor A, Bolay H, Andermann ML, Moskowitz MA, Dale AM, et al. Simultaneous imaging of total cerebral hemoglobin concentration, oxygenation, and blood flow during functional activation. Opt Lett [Internet]. 2003;28(1):28–30.
2. Devor A, Dunn AK, Andermann ML, Ulbert I, Boas DA, Dale AM. Coupling of total hemoglobin concentration, oxygenation, and neural activity in rat somatosensory cortex. Neuron. 2003;39(2):353–9.
3. Wright GA, Hu BS, Macovski A. Estimating oxygen saturation of blood in vivo with MR imaging at 1.5 T. J Magn Reson Imaging [Internet]. 1991;1(3):275–83. https://doi.org/10.1002/jmri.1880010303.
4. An H, Lin W. Quantitative measurements of cerebral blood oxygen saturation using magnetic resonance imaging. J Cereb Blood Flow Metab [Internet]. 2000;20(8):1225–36. https://doi.org/10.1097/00004647-200008000-00008.
5. Axel L. Blood flow effects in magnetic resonance imaging. Am J Roentgenol [Internet]. 1984;143(6):1157–66. https://doi.org/10.2214/ajr.143.6.1157.
6. Shung KK. Diagnostic ultrasound: imaging and blood flow measurements. Boca Raton: CRC Press; 2005.
7. Carreau A, El H-R, Matejuk A, Grillon C, Kieda C. Why is the partial oxygen pressure of human tissues a crucial parameter? Small molecules and hypoxia. J Cell Mol Med [Internet]. 2011;15(6):1239–53. https://doi.org/10.1111/j.1582-4934.2011.01258.x.
8. de Jonge E, Peelen L, Keijzers PJ, Joore H, de Lange D, van der Voort PHJ, et al. Association between administered oxygen, arterial partial oxygen pressure and mortality in mechanically ventilated intensive care unit patients. Crit Care [Internet]. 2008;12(6):R156. https://doi.org/10.1186/cc7150.
9. He X, Zhu M, Yablonskiy DA. Validation of oxygen extraction fraction measurement by qBOLD technique. Magn Reson Med [Internet]. 2008;60(4):882–8.
10. Golay X, Silvennoinen MJ, Zhou J, Clingman CS, Kauppinen RA, Pekar JJ, et al. Measurement of tissue oxygen extraction ratios from venous blood T2: increased precision and validation of principle. Magn Reson Med [Internet]. 2001;46(2):282–91. https://doi.org/10.1002/mrm.1189.
11. Powers WJ, Grubb RL Jr, Darriet D, Raichle ME. Cerebral blood flow and cerebral metabolic rate of oxygen requirements for cerebral function and viability in humans. J Cereb Blood Flow Metab. 1985;5(4):600–8.
12. Yamaguchi T, Kanno I, Uemura K, Shishido F, Inugami A, Ogawa T, et al. Reduction in regional cerebral metabolic rate of oxygen during human aging. Stroke. 1986;17(6):1220–8.
13. Merla A, Romani GL (2006) Biomedical applications of functional infrared imaging. In: 2005 IEEE engineering in medicine and biology 27th annual conference. IEEE; 2006, pp 690–693.
14. Dhawan AP, D'Alessandro B, Fu X. Optical imaging modalities for biomedical applications. IEEE Rev Biomed Eng. 2010;3:69–92.
15. Godik EE, Gulyaev YV. Functional imaging of the human body. IEEE Eng Med Biol Mag. 1991;10(4):21–9.
16. Pacak K, Eisenhofer G, Goldstein DS. Functional imaging of endocrine tumors: role of positron emission tomography. Endocr Rev. 2004;25(4):568–80.
17. Axel L. Cerebral blood flow determination by rapid-sequence computed tomography: theoretical analysis. Radiology. 1980;137(3):679–86.
18. Huettel SA, Song AW, McCarthy G. Functional magnetic resonance imaging, vol. 1. Sunderland: Sinauer Associates; 2004.
19. Yücel MA, Selb JJ, Huppert TJ, Franceschini MA, Boas DA. Functional near infrared spectroscopy: enabling routine functional brain imaging. Curr Opin Biomed Eng. 2017;4:78–86.
20. Wang LV, Wu H. Biomedical optics: principles and imaging. New York: Wiley; 2007.
21. Yao J, Wang LV. Photoacoustic microscopy. Laser Photon Rev. 2013;7(5):758–78.
22. Jang H-Y, Kim H-R, Kang M-S, Kim M-H, Zhang B-T. The demand for quantitative techniques in biomedical image informatics. Biomed Eng Lett. 2014;4(4):319–27.
23. Lecchi M, Fossati P, Elisei F, Orecchia R, Lucignani G. Current concepts on imaging in radiotherapy. Eur J Nucl Med Mol Imaging. 2008;35(4):821–37.
24. Liu K, Li J, Raghunathan R, Zhao H, Li X, Wong STC (2021) The progress of label-free optical imaging in alzheimer's disease screening and diagnosis. Front Aging Neurosci 2021;3:455.
25. Wang LV, Yao J. A practical guide to photoacoustic tomography in the life sciences. Nat Methods. 2016;13(8):627.
26. Yin C, Wen G, Liu C, Yang B, Lin S, Huang J et al (2018) Organic semiconducting polymer nanoparticles for photoacoustic labelling and tracking of stem cells in the second near-infrared window. ACS Nano. 2018;12(12):12201–11.
27. Zhang J, Wen G, Wang W, Cheng K, Guo Q, Tian S, et al. Controllable cleavage of C–N bond-based fluorescent and photoacoustic dual-modal probes for the detection of H2S in living mice. ACS Appl Bio Mater. 2021;4(3):2020–5.
28. Wen G, Li X, Zhang Y, Han X, Xu X, Liu C, et al. Effective phototheranostics of brain tumor assisted by near-infrared-II light-responsive semiconducting polymer nanoparticles. ACS Appl Mater Interfaces. 2020;12(30):33492–9.
29. Yu J, Wang Q, Li M, Liu C, Wang L, Xu T, et al. Characterizing nanoparticle swarms with tuneable concentrations for enhanced imaging contrast. IEEE Robot Autom Lett. 2019;4(3):2942–9.
30. Zhang Y, Wang Y, Lai P, Wang L. Video-rate dual-modal wide-beam harmonic ultrasound and photoacoustic computed tomography. IEEE Trans Med Imaging. 2022;41(3):727–36.
31. Li D, Zhang Y, Liu C, Chen J, Sun D, Wang L. Review of photoacoustic imaging for microrobots tracking in vivo [Invited]. Chin Opt Lett [Internet]. 2021;19(11):111701.

32. Zhou Y, Liu C, Huang X, Qian X, Wang L, Lai P. Low-consumption photoacoustic method to measure liquid viscosity. Biomed Opt Express. 2021;12(11):7139–48.

33. Hosseinaee Z, Le M, Bell K, Reza PH. Towards non-contact photoacoustic imaging [review]. Photoacoustics [Internet]. 2020;20:100207.

34. Zhang Y, Wang L. Video-rate ring-array ultrasound and photoacoustic tomography. IEEE Trans Med Imaging. 2020;39(12):4369–75.

35. Qi S, Zhang Y, Liu G, Chen J, Li X, Zhu Q et al. Plasmonic-doped melanin-mimic for CXCR4-Targeted NIR-II photoacoustic computed tomography-guided photothermal ablation of orthotopic hepatocellular carcinoma. Acta Biomater. 2021;129:245–57.

36. Wang K, Li C, Chen R, Shi J. Recent advances in high-speed photoacoustic microscopy. Photoacoustics [Internet]. 2021;24:100294.

37. Li J, Yao Y, Jiang L, Li S, Yi Z, Chen X, et al. Time-domain terahertz optoacoustics: manipulable water sensing and dampening. Adv Photonics. 2021;3(2):26003.

38. Ahn J, Kim JY, Choi W, Kim C. High-resolution functional photoacoustic monitoring of vascular dynamics in human fingers. Photoacoustics. 2021;23:100282.

39. Kim J, Park B, Ha J, Steinberg I, Hooper SM, Jeong C et al. Multiparametric photoacoustic analysis of human thyroid cancers in vivo. Cancer Res. 2021;81(18):4849–60.

40. Park J, Park B, Kim TY, Jung S, Choi WJ, Ahn J, et al. Quadruple fusion imaging via transparent ultrasound transducer: ultrasound, photoacoustic, optical coherence, and fluorescence imaging. Proc Natl Acad Sci USA. 2021;118(11):e1920879118.

41. Lee C, Choi W, Kim J, Kim C. Three-dimensional clinical handheld photoacoustic/ultrasound scanner. Photoacoustics. 2020;18:100173.

42. Kim J, Kim JY, Jeon S, Baik JW, Cho SH, Kim C. Super-resolution localization photoacoustic microscopy using intrinsic red blood cells as contrast absorbers. Light Sci Appl. 2019;8(1):1–11.

43. Jeon S, Kim J, Lee D, Baik JW, Kim C. Review on practical photoacoustic microscopy. Photoacoustics [Internet]. 2019;15:100141.

44. Jeon S, Choi W, Park B, Kim C. A deep learning-based model that reduces speed of sound aberrations for improved in vivo photoacoustic imaging. IEEE Trans Image Process. 2021;30:8773–84.

45. Cho S-W, Park SM, Park B, Lee TG, Kim B-M, Kim C, et al. High-speed photoacoustic microscopy: A review dedicated on light sources. Photoacoustics. 2021;24:100291.

46. Chen M, Duan X, Lan B, Vu T, Zhu X, Rong Q, et al. High-speed functional photoacoustic microscopy using a water-immersible two-axis torsion-bending scanner. Photoacoustics. 2021;24:100309.

47. Zangabad RP, Iskander-Rizk S, van der Meulen P, Meijlink B, Kooiman K, Wang T, et al. Photoacoustic flow velocity imaging based on complex field decorrelation. Photoacoustics. 2021;22:100256.

48. Chen J, Zhang Y, Bai S, Zhu J, Chirarattananon P, Ni K, et al. Dual-foci fast-scanning photoacoustic microscopy with 3.2-MHz A-line rate. Photoacoustics [Internet]. 2021;23:100292.

49. Li M, Tang Y, Yao J. Photoacoustic tomography of blood oxygenation: a mini review. Photoacoustics. 2018;10:65–73.

50. Van den Berg PJ, Daoudi K, Steenbergen W. Review of photoacoustic flow imaging: its current state and its promises. Photoacoustics. 2015;3(3):89–99.

51. Gehrung M, Bohndiek SE, Brunker J. Development of a blood oxygenation phantom for photoacoustic tomography combined with online pO$_2$ detection and flow spectrometry. J Biomed Opt. 2019;24(12):121908.

52. Deng Z, Wang Z, Yang X, Luo Q, Gong H. In vivo imaging of hemodynamics and oxygen metabolism in acute focal cerebral ischemic rats with laser speckle imaging and functional photoacoustic microscopy. J Biomed Opt. 2012;17(8):81415.

53. Liu T, Wei Q, Wang J, Jiao S, Zhang HF. Combined photoacoustic microscopy and optical coherence tomography can measure metabolic rate of oxygen. Biomed Opt Express. 2011;2(5):1359–65.

54. Li C, Hu S, Maslov K, Wang LV. Optical-resolution photoacoustic microscopy. Focus Microsc. 2009;59:7693–7693.

55. Liu C, Chen J, Zhang Y, Zhu J, Wang L. Five-wavelength optical-resolution photoacoustic microscopy of blood and lymphatic vessels. Adv Photon [Internet]. 2021 Jan 1;3(1):1–10. https://doi.org/10.1117/1.AP.3.1.016002.

56. Li X, Kang L, Zhang Y, Wong TTW. High-speed label-free ultraviolet photoacoustic microscopy for histology-like imaging of unprocessed biological tissues. Opt Lett. 2020;45(19):5401–4.

57. Zhou Y, Chen J, Liu C, Liu C, Lai P, Wang L. Single-shot linear dichroism optical-resolution photoacoustic microscopy. Photoacoustics. 2019;16:100148.

58. Li D, Liu C, Yang Y, Wang L, Shen Y. Micro-rocket robot with all-optic actuating and tracking in blood. Light Sci Appl. 2020;9(1):1–10.

59. Chen J, Zhang Y, He L, Liang Y, Wang L (2020) Wide-field polygon-scanning photoacoustic microscopy of oxygen saturation at 1-MHz A-line rate. Photoacoustics. 2020;20:100195.

60. Li X, Kot JCK, Tsang VTC, Lo CTK, Huang B, Tian Y, et al. Ultraviolet photoacoustic microscopy with tissue clearing for high-contrast histological imaging. Photoacoustics [Internet]. 2022;25:100313.

61. Qin W, Gan Q, Yang L, Wang Y, Qi W, Ke B, et al. High-resolution in vivo imaging of rhesus cerebral cortex with ultrafast portable photoacoustic microscopy. Neuroimage [Internet]. 2021;238: 118260. https://doi.org/10.1016/j.neuroimage.2021.118260.

62. Liu C, Liang Y, Wang L. Optical-resolution photoacoustic microscopy of oxygen saturation with nonlinear compensation. Biomed Opt Express. 2019;10(6):3061.

63. Shemetov AA, Monakhov MV, Zhang Q, Canton-Josh JE, Kumar M, Chen M, et al. A near-infrared genetically encoded calcium indicator for in vivo imaging. Nat Biotechnol. 2021;39(3):368–77.

64. Yao J, Maslov KI, Shi Y, Taber LA, Wang LV. In vivo photoacoustic imaging of transverse blood flow by using Doppler broadening of bandwidth. Opt Lett. 2010;35(9):1419–21.

65. Sun N, Zheng S, Rosin DL, Poudel N, Yao J, Perry HM, et al. Development of a photoacoustic microscopy technique to assess peritubular capillary function and oxygen metabolism in the mouse kidney. Kidney Int [Internet]. 2021;100(3):613–20. https://doi.org/10.1016/j.kint.2021.06.018.

66. Wang Y, Hu S, Maslov K, Zhang Y, Xia Y, Wang LV. In vivo integrated photoacoustic and confocal microscopy of hemoglobin oxygen saturation and oxygen partial pressure. Opt Lett. 2011;36(7):1029.

67. Chen J, Zhang Y, Li X, Zhu J, Li D, Li S, et al. Confocal visible/NIR photoacoustic microscopy of tumors with structural, functional, and nanoprobe contrasts. Photon Res. 2020;8(12):1875–80.

68. Da Mesquita S, Louveau A, Vaccari A, Smirnov I, Cornelison RC, Kingsmore KM, et al. Functional aspects of meningeal lymphatics in ageing and Alzheimer's disease. Nature [Internet]. 2018;560(7717):185–91. https://doi.org/10.1038/s41586-018-0368-8.

69. Wang T, Sun N, Cao R, Ning B, Chen R, Zhou Q, et al. Multiparametric photoacoustic microscopy of the mouse brain with 300-kHz A-line rate. Neurophotonics. 2016;3(4):045006.

70. Liang Y, Jin L, Guan BO, Wang L. 2 MHz multi-wavelength pulsed laser for functional photoacoustic microscopy. Opt Lett. 2017;42(7):1452–1455.

71. He Y, Shi J, Maslov KI, Cao R, Wang LV. Wave of single-impulse-stimulated fast initial dip in single vessels of mouse brains imaged by high-speed functional photoacoustic microscopy. J Biomed Opt. 2020;25(06):1.

72. Hosseinaee Z, Ecclestone B, Pellegrino N, Khalili L, Mukhangaliyeva L, Fieguth P, et al. Functional photoacoustic remote sensing microscopy using a stabilized temperature-regulated stimulated Raman scattering light source. Opt Express. 2021;29(19):29745.

73. Ning B, Kennedy MJ, Dixon AJ, Sun N, Cao R, Soetikno BT et al. Simultaneous photoacoustic microscopy of microvascular anatomy, oxygen saturation, and blood flow. Opt Lett. 2015;40(6):910–913

74. Danielli A, Favazza CP, Maslov K, Wang LV. Single-wavelength functional photoacoustic microscopy in biological tissue. Opt Lett. 2011;36(5):769.

75. Yao J, Wang L, Yang JM, Maslov KI, Wong TTW, Li L, et al. High-speed label-free functional photoacoustic microscopy of mouse brain in action. Nat Methods. 2015;12(5):407–10.

76. Zhu J, Liu C, Liu Y, Chen J, Zhang Y, Yao K, et al. Self-fluence-compensated functional photoacoustic microscopy. IEEE Trans Med Imaging. 2021;20(10):1–11.

77. Liang Y, Liu H, Li Q, Jin L, Guan B-O, Wang L. Acoustic-spectrum-compensated photoacoustic microscopy. Opt Lett. 2020;45(7):1850.

78. Hajireza P, Forbrich A, Zemp R. In-vivo functional optical-resolution photoacoustic microscopy with stimulated Raman scattering fiber-laser source. Biomed Opt Express [Internet]. 2014;5(2):539.

79. Danielli A, Favazza CP, Maslov K, Wang LV. Picosecond absorption relaxation measured with nanosecond laser photoacoustics. Appl Phys Lett. 2010;97(16):163701.

80. Wang J, Liu T, Jiao S, Chen R, Zhou Q, Shung KK, et al. Saturation effect in functional photoacoustic imaging. J Biomed Opt [Internet]. 2010;15(2):021317. https://doi.org/10.1117/1.3333549.

81. Kumon RE, Deng CX, Wang X. Frequency-domain analysis of photoacoustic imaging data from prostate adenocarcinoma tumors in a murine model. Ultrasound Med Biol. 2011;37(5):834–9.

82. Tilles AW, Eckstein EC. The near-wall excess of platelet-sized particles in blood flow: its dependence on hematocrit and wall shear rate. Microvasc Res. 1987;33(2):211–23.

83. Zhang P, Yu H, Zhou N, Zhang J, Wu Y, Zhang Y, et al. Early exercise improves cerebral blood flow through increased angiogenesis in experimental stroke rat model. J Neuroeng Rehabil. 2013;10(1):1–10.

84. Kohner EM, Hamilton AM, Saunders SJ, Sutcliffe BA, Bulpitt CJ. The retinal blood flow in diabetes. Diabetologia. 1975;11(1):27–33.

85. Yonas H, Smith HA, Durham SR, Pentheny SL, Johnson DW. Increased stroke risk predicted by compromised cerebral blood flow reactivity. J Neurosurg. 1993;79(4):483–9.

86. Craig AH, Cummings JL, Fairbanks L, Itti L, Miller BL, Li J, et al. Cerebral blood flow correlates of apathy in Alzheimer disease. Arch Neurol. 1996;53(11):1116–20.

87. Srinivasan VJ, Sakadžić S, Gorczynska I, Ruvinskaya S, Wu W, Fujimoto JG, et al. Quantitative cerebral blood flow with optical coherence tomography. Opt Express. 2010;18(3):2477–94.

88. Gill RW. Measurement of blood flow by ultrasound: accuracy and sources of error. Ultrasound Med Biol. 1985;11(4):625–41.

89. Hoskins PR. Measurement of arterial blood flow by Doppler ultrasound. Clin Phys Physiol Meas. 1990;11(1):1.

90. Boas DA, Dunn AK. Laser speckle contrast imaging in biomedical optics. J Biomed Opt. 2010;15(1):11109.

91. Wang L, Maslov K, Yao J, Rao B, Wang LV. Fast voice-coil scanning optical-resolution photoacoustic microscopy. Opt Lett. 2011;36(2):139–41.

92. Wang L, Maslov K, Wang LV. Single-cell label-free photoacoustic flowoxigraphy in vivo. Proc Natl Acad Sci. 2013;110(15):5759–64.

93. Fang H, Maslov K, Wang LV. Photoacoustic Doppler effect from flowing small light-absorbing particles. Phys Rev Lett. 2007;99(18):184501.

94. Fang H, Maslov K, Wang LV. Photoacoustic Doppler flow measurement in optically scattering media. Appl Phys Lett. 2007;91(26):3–6.

95. Sheinfeld A, Gilead S, Eyal A. Simultaneous spatial and spectral mapping of flow using photoacoustic Doppler measurement. J Biomed Opt. 2010;15(6):066010.

96. Sheinfeld A, Gilead S, Eyal A. Photoacoustic Doppler measurement of flow using tone burst excitation. Opt Express. 2010;18(5):4212.

97. Zhang R, Yao J, Maslov KI, Wang LV. Structured-illumination photoacoustic Doppler flowmetry of axial flow in homogeneous scattering media. Appl Phys Lett. 2013;103(9):094101.

98. Yao J, Gilson RC, Maslov KI, Wang L, Wang LV. Calibration-free structured-illumination photoacoustic flowgraphy of transverse flow in scattering media. J Biomed Opt. 2014;19(4):046007.

99. Yao J, Wang LV. Transverse flow imaging based on photoacoustic Doppler bandwidth broadening. J Biomed Opt. 2010;15(2):21304.

100. Qiao W, Chen Z, Zhou W, Xing D. All-optical photoacoustic Doppler transverse blood flow imaging. Opt Lett. 2018;43(11):2442–5.

101. Chen S, Ling T, Huang S, Baac HW, Guo LJ. Photoacoustic correlation spectroscopy and its application to low-speed flow measurement. Opt Lett. 2010;35(8):1200–2

102. Köhler RH, Schwille P, Webb WW, Hanson MR. Active protein transport through plastid tubules: velocity quantified by fluorescence correlation spectroscopy. J Cell Sci. 2000;113(22):3921–30.

103. Chen S, Xie Z, Carson PL, Wang X, Guo LJ. In vivo flow speed measurement of capillaries by photoacoustic correlation spectroscopy. Opt Lett. 2011;36(20):4017–9

104. Tay JW, Liang J, Wang LV. Amplitude-masked photoacoustic wavefront shaping and application in flowmetry. Opt Lett. 2014;39(19):5499.

105. Brunker J, Beard P. Pulsed photoacoustic Doppler flowmetry using time-domain cross-correlation: Accuracy, resolution and scalability. J Acoust Soc Am. 2012;132(3):1780–91.

106. Brunker J, Beard P. Acoustic resolution photoacoustic Doppler flowmetry: practical considerations for obtaining accurate measurements of blood flow. Photons Plus Ultrasound Imaging Sens. 2014;2014(8943):89431K.

107. Brunker J, Beard P. Velocity measurements in whole blood using acoustic resolution photoacoustic. Doppler. 2016;7(7):89–99.

108. Liang J, Zhou Y, Maslov KI, Wang LV. Cross-correlation-based transverse flow measurements using optical resolution photoacoustic microscopy with a digital micromirror device. J Biomed Opt. 2013;18(9):096004.

109. Zhou Y, Liang J, Maslov KI, Wang LV. Calibration-free in vivo transverse blood flowmetry based on cross correlation of slow time profiles from photoacoustic microscopy. Opt Lett. 2013;38(19):3882.

110. Carter LP. Thermal diffusion flowmetry. Neurosurg Clin N Am. 1996;7(4):749–54.

111. Sheinfeld A, Eyal A. Photoacoustic thermal diffusion flowmetry. Biomed Opt Express. 2012;3(4):2610–2.

112. Wang L, Yao J, Maslov KI, Xing W, Wang LV. Ultrasound-heated photoacoustic flowmetry. J Biomed Opt. 2013;18(11):117003.

113. Wang L, Xia J, Yao J, Maslov KI, Wang LV. Ultrasonically encoded photoacoustic flowgraphy in biological tissue. Phys Rev Lett. 2013;111(20):1–5.

114. Zhang R, Wang L, Yao J, Yeh C-H, Wang LV. In vivo optically encoded photoacoustic flowgraphy. Opt Lett. 2014;39(13):3814–7.

115. Liu W, Lan B, Hu L, Chen R, Zhou Q, Yao J. Photoacoustic thermal flowmetry with a single light source. J Biomed Opt. 2017;22(9):96001.

116. Liu C, Liang Y, Wang L. Single-shot photoacoustic microscopy of hemoglobin concentration, oxygen saturation, and blood flow in sub-microseconds. Photoacoustics. 2020;17:100156.

117. Ortiz-Prado E, Dunn JF, Vasconez J, Castillo D, Viscor G. Partial pressure of oxygen in the human body: a general review. Am J Blood Res [Internet]. 2019;9(1):1–14.

118. De Santis V, Singer M. Tissue oxygen tension monitoring of organ perfusion: Rationale, methodologies, and literature review. Br J Anaesth [Internet]. 2015;115(3):357–65. https://doi.org/10.1093/bja/aev162.

119. Rich LJ, Seshadri M. Photoacoustic monitoring of tumor and normal tissue response to radiation. Sci Rep [Internet]. 2016;6(1):21237. https://doi.org/10.1038/srep21237.

120. Helmlinger G, Yuan F, Dellian M, Jain RK. Interstitial pH and pO 2 gradients in solid tumors in vivo: high-resolution measurements reveal a lack of correlation. Nat Med. 1997;3(2):177–82.

121. Ashkenazi S. Photoacoustic lifetime imaging of dissolved oxygen using methylene blue. J Biomed Opt. 2010;15(4):040501.

122. Shao Q, Morgounova E, Jiang C, Choi J, Bischof J, Ashkenazi S. In vivo photoacoustic lifetime imaging of tumor hypoxia in small animals. J Biomed Opt. 2013;18(7):076019.

123. Shao Q, Ashkenazi S. Photoacoustic lifetime imaging for direct in vivo tissue oxygen monitoring. J Biomed Opt. 2015;20(3):036004.

124. Huang S, Eary JF, Jia C, Huang L, Ashkenazi S, Donnell MO. Differential-absorption photoacoustic imaging. Opt Lett. 2009;34(16):2393–5.

125. Stylogiannis A, Riobo L, Prade L, Glasl S, Klein S, Lucidi G, et al. Low-cost single-point optoacoustic sensor for spectroscopic measurement of local vascular oxygenation. Opt Lett. 2020;45(24):6579.

126. Friedrich CS, Mienkina MP, Brenner C, Gerhardt NC, Jörger M, Strauß A, et al. Quantitative photoacoustic blood oxygenation measurement of whole porcine blood samples using a multi-wavelength semiconductor laser system. Opt InfoBase Conf Pap. 2011;8088:1–9.

127. Gröhl J, Kirchner T, Adler TJ, Hacker L, Holzwarth N, Hernández-Aguilera A, et al. Learned spectral decoloring enables photoacoustic oximetry. Sci Rep [Internet]. 2021;11(1):1–12. https://doi.org/10.1038/s41598-021-83405-8.

128. Needles A, Heinmiller A, Sun J, Theodoropoulos C, Bates D, Hirson D, et al. Development and initial application of a fully integrated photoacoustic micro-ultrasound system. IEEE Trans Ultrason Ferroelectr Freq Control. 2013;60(5):888–97.

129. Vanderkooi JM, Wilson DF. A new method for measuring oxygen concentration in biological systems. In: Oxygen transport to tissue VIII. Boston, MA: Springer; 1986. p. 189–93.

130. Forbrich A, Shao P, Shi W, Zemp RJ. Lifetime-weighted photoacoustic imaging. J.Opt. 2016;18(12):124001.

131. Lo LW, Koch CJ, Wilson DF. Calibration of oxygen-dependent quenching of the phosphorescence of Pd-meso-tetra (4-carboxyphenyl) porphine: a phosphor with general application for measuring oxygen concentration in biological systems. Anal Biochem. 1996;236(1):153–60.

132. Sinaasappel M, Ince C. Special communication. JAMA J Am Med Assoc. 1963;184(1):47.

133. Xie S. MR OEF imaging in MELAS [Internet], 1st ed. Vol. 547, Methods in Enzymology. Elsevier Inc.; 2014. 433–444 p. https://doi.org/10.1016/B978-0-12-801415-8.00021-7

134. Hu S, Gonzales E, Soetikno B, Gong E, Yan P, Maslov K, et al. Optical-resolution photoacoustic microscopy of ischemic stroke. Photons Plus Ultrasound Imaging Sens. 2011;7899:789906.

135. Cao R, Li J, Kharel Y, Zhang C, Morris E, Santos WL, et al. Photoacoustic microscopy reveals the hemodynamic basis of sphingosine 1-phosphate-induced neuroprotection against ischemic stroke. Theranostics. 2018;8(22):6111–20.

136. Cao R, Zhang C, Mitkin VV, Lankford MF, Li J, Zuo Z, et al. Comprehensive characterization of cerebrovascular dysfunction in blast traumatic brain injury using photoacoustic microscopy. J Neurotrauma. 2019;36:1526–34.

137. Krumholz A, Wang L, Yao J, Wang LV. Functional photoacoustic microscopy of diabetic vasculature. J Biomed Opt. 2012;17(6):060502.

138. Cao R, Tran A, Li J, Xu Z, Sun N, Zuo Z, et al. Hemodynamic and oxygen-metabolic responses of the awake mouse brain to hypercapnia revealed by multi-parametric photoacoustic microscopy. J Cereb Blood Flow Metab. 2021;41(10):2628–39.

139. Cao R, Li J, Zhang C, Zuo Z, Hu S. Photoacoustic microscopy of obesity-induced cerebrovascular alterations. Neuroimage [Internet]. December 2018;2019(188):369–79. https://doi.org/10.1016/j.neuroimage.2018.12.027.

140. Boushel R, Langberg H, Olesen J, Gonzales-Alonzo J, Bülow J, Kjaer M. Monitoring tissue oxygen availability with near infrared spectroscopy (NIRS) in health and disease. Scand J Med Sci Sports. 2001;11(4):213–22.

141. Diringer MN, Aiyagari V, Zazulia AR, Videen TO, Powers WJ. Effect of hyperoxia on cerebral metabolic rate for oxygen measured using positron emission tomography in patients with acute severe head injury. J Neurosurg. 2007;106(4):526–9.

142. Xu F, Ge Y, Lu H. Noninvasive quantification of whole-brain cerebral metabolic rate of oxygen (CMRO2) by MRI. Magn Reson Med. 2009;62(1):141–8.

143. Yao J, Maslov KI, Zhang Y, Xia Y, Wang LV. Label-free oxygen-metabolic photoacoustic microscopy in vivo. J Biomed Opt. 2011;16(7):076003.

144. Ni R, Rudin M, Klohs J. Cortical hypoperfusion and reduced cerebral metabolic rate of oxygen in the arcAβ mouse model of Alzheimer's disease. Photoacoustics [Internet]. 2018;10:38–47. https://doi.org/10.1016/j.pacs.2018.04.001.

145. Cao R, Li J, Ning B, Sun N, Wang T, Zuo Z, et al. Functional and oxygen-metabolic photoacoustic microscopy of the awake mouse brain. Neuroimage [Internet]. 2017;150:77–87.

Publisher's Note Springer Nature remains neutral with regard to jurisdictional claims in published maps and institutional affiliations.